A New TKE-Based Parameterization of Atmospheric Turbulence in the Canadian Global and Regional Climate Models

Y. He, N.A. McFarlane, and A.H. Monahan

May 2019

This article was originally published at:
https://doi.org/10.1029/2018MS001532

JAMES | Journal of Advances in Modeling Earth Systems

RESEARCH ARTICLE
10.1029/2018MS001532

A New TKE-Based Parameterization of Atmospheric Turbulence in the Canadian Global and Regional Climate Models

Y. He[1], N. A. McFarlane[2,3], and A. H. Monahan[2]

[1]Pacific Climate Impacts Consortium, University of Victoria, Victoria, British Columbia, Canada, [2]School of Earth and Ocean Sciences, University of Victoria, Victoria, British Columbia, Canada, [3]Canadian Centre For Climate Modelling and Analysis, University of Victoria, Victoria, British Columbia, Canada

Key Points:

- The new TKE parameterization accounts for nonlocal turbulent transfer of heat and moisture and scalar constituents in convectively active atmospheric boundary layers in terms of relaxation to characteristic vertical profiles
- The new TKE scheme includes an innovative representation of the turbulent Prandtl number and turbulent diffusivities for both convectively active and stably stratified conditions in both cloudy and clear atmospheric boundary layers
- The new TKE scheme is implemented and tested in a single-column model; results for selected atmospheric boundary layer regimes are compared with observations and published LES results

Correspondence to:
N. A. McFarlane,
normanmc@uvic.ca

Citation:
He, Y., McFarlane, N. A., & Monahan, A. H. (2019). A new TKE-based parameterization of atmospheric turbulence in the Canadian global and regional climate models. *Journal of Advances in Modeling Earth Systems*, *11*, 1153–1188. https://doi.org/10.1029/2018MS001532

Received 17 OCT 2018
Accepted 11 MAR 2019
Accepted article online 20 MAR 2019
Published online 3 MAY 2019

Abstract A new semi-empirical turbulence parameterization is presented. Key features of the scheme include representation of turbulent diffusivities in terms of the turbulent kinetic energy that is determined by solving a quasi-equilibrium form of the equation representing the turbulent kinetic energy budget. The new parameterization is innovative in the treatment of turbulent transfer in stably stratified conditions and the representation of nonlocal contributions to the vertical transport of heat, moisture, and scalar prognostic variables in convectively active boundary layers. A key element in the modeling of turbulence in stably stratified conditions is the formulation of the turbulent Prandtl number based on the results of recently published theoretical, modeling, and observational studies of stratified turbulence in the atmospheric boundary layer. The new parameterization has been implemented in the CanAM4 single column model. Its performance in comparison with that of the operational CanAM4 turbulence parameterization is documented in terms of selected results from case studies for clear-sky conditions based on meteorological observations from the KNMI-mast at Cabauw, Netherlands, and the Second Dynamics and Chemistry of Marine Stratocumulus case study of stratocumulus-topped marine boundary layers. The performance of the new and operational schemes is qualitatively similar in clear-sky conditions in both convective and stable boundary layer regimes. However, they perform differently for the extended simulations for the Second Dynamics and Chemistry of Marine Stratocumulus case study. The new scheme maintains an elevated stratocumulus layer throughout a 30-hr simulation, but peak liquid water contents are larger than large eddy simulations.

Plain Language Summary This paper presents a new mathematical formulation to account for the effects turbulent motions in comprehensive global climate models. The new formulation is based on recently published theoretical advances and results of high-resolution numerical model simulations for specialized atmospheric turbulence regimes. The new formulation is tested and evaluated using a simplified model configuration designed to represent a single grid volume of a global climate model.

1. Introduction

The comprehensive numerical models that are used for climate simulation within the Canadian Centre for Climate Modeling and Analysis have become increasingly complex over the last four decades. Although the treatment of atmospheric boundary layer processes within these models has also evolved with time (von Salzen et al., 2013), the basic formulations used to account for turbulent transfer processes have not changed significantly over the last two decades. In common with other similar global climate models (GCMs), the current treatments do not explicitly deal with some of the complex processes within the atmospheric boundary layer, such as the coupling between turbulence and cloud processes that occurs within extensive stratocumulus-topped marine boundary layers that commonly occur in coastal regions. It is now widely recognized that such processes play a key role in the radiation budget and hydrological cycle of the global climate system.

Stably stratified boundary layers are another frontier in atmospheric research. Traditional treatments of turbulent transfer in stably stratified atmospheric regimes in operation models used for weather and climate prediction have been based on turbulent closure formulations that typically predict that turbulence

ceases in moderately stable conditions where the local gradient Richardson number exceeds some critical value that is less than unity. It has long been recognized, however, that allowing this to happen in numerical models often results in undesirable and spurious effects such as decoupling between atmosphere and surface accompanied by excessive cooling of land surfaces in statically stable regimes. Ad hoc modifications of formulations for stable regimes intended to soften such effects have commonly been invoked to deal with such problems. These typically involve retaining weak turbulent diffusion in stable conditions.

A heuristic justification for such practices is that the coarse spatial and temporal resolution employed in such models limits their ability to resolve or adequately represent processes that give rise to spatially and temporally localized turbulence that may exist in the presence of the resolved larger-scale stably stratified mean state. While this is certainly an abiding issue for operational weather and climate models, it is also now well recognized, on the basis of observations, theoretical, and modeling studies, that turbulence can and does exist in circumstances where the background stratification is sufficiently stable that the gradient Richardson number exceeds unity. In recent years such stably stratified flow regimes in the atmospheric boundary layer have been studied extensively. These studies include both observational campaigns and theoretical investigations based on large eddy simulations (LES) and higher-order closure (HOC) turbulence modeling.

In the context of HOC modeling, the pioneering studies of Zilitinkevich et al. (2007) and Canuto et al. (2008) have demonstrated that turbulence models that do not include a critical Richardson number cutoff can be consistently formulated. Canuto et al. (2008) discuss the physical underpinnings for such models. More recently, studies such as those of Kantha and Carniel (2009), Venayagamoorthy and Stretch (2010), and Ferrero et al. (2011) substantially support and elucidate these earlier studies.

These works have inspired and informed the simplified semi-empirical turbulence scheme that is developed in the present work, which was undertaken as part of a collaborative research program within the Canadian Network for Regional Climate and Weather Processes. The main objective of this subproject has been to develop improved parameterizations of physical processes for use in newer versions of the Canadian global and regional climate models that are currently under development and/or planned for the near future.

The turbulence scheme documented in this paper is a further development and elaboration of that presented in the supplement to He et al. (2012). The formulation of the turbulence scheme is outlined in sections 2 to 7 of this paper. Results of single column model (SCM) tests of the new scheme and comparison with the current operational scheme used in CanAM4 (von Salzen et al., 2013) are discussed in section 8, followed by a general discussion and conclusions in section 9. Appendix 1 provides details of the solution of the turbulent kinetic energy (TKE) equation. Appendix 2 provides a summary and update on the procedure, documented in more detail by Abdella and McFarlane (1996), for determining surface fluxes in terms of prognostic variables at the lowest model level.

2. Basic Formulation Based on the Turbulent Kinetic Energy Budget

As documented in von Salzen et al. (2013) the operational turbulent transfer scheme in CanAM4 is a simple first-order scheme in which diffusivities are of the general form $K = \ell^2 \left|\partial \vec{V}/\partial z\right| f(Ri)$, where Ri is the gradient Richardson number. The location of the top of the boundary layer is defined as the level above which the gradient Richardson number first exceeds unity.

The functions $f(Ri)$ are specified empirically and separately for momentum and scalar prognostic variables with differing functional forms over land and ocean. The effective Prandtl number is unity for stable conditions ($Ri \geq 0$) for this scheme. The mixing length in the boundary layer has upward and downward components that are simply proportional, respectively, to the height above the surface and the distance to the top of the boundary layer. Above the boundary layer the neutral mixing lengths decrease from the value at the top of the boundary layer to a limiting value of 10 m as a function of $(p/p_t)^2$, where p is the ambient large-scale pressure and p_t is the value at the top of the boundary layer. A notable shortcoming of the operational turbulent transfer scheme is that it typically does not represent the effects of entrainment at the top of convectively active boundary layers in a realistic manner.

The surface layer treatment is as documented in Abdella and McFarlane (1996) but was developed and implemented independently of the formulation for the rest of the boundary layer and the free atmosphere. As discussed in more detail below, the operational CanAM4 boundary layer scheme also includes a simple parameterization of nonlocal turbulent transfer of scalar prognostic quantities in the boundary layer in convectively active conditions.

The new scheme documented herein is designed to parameterize turbulent transfer in a self-consistent manner for all of the model prognostic variables at all model levels based on a TKE budget and also takes into account key developments in atmospheric turbulence research in recent years.

Following a traditional basic approach, vertical fluxes are defined in terms of eddy diffusivities as

$$\left(\overline{u'w'}, \overline{v'w'}\right) = -K_m\left(\frac{\partial U}{\partial x}, \frac{\partial V}{\partial z}\right) \tag{1a}$$

$$\overline{w'\theta'_v} = -K_h\frac{\partial \theta_v}{\partial z} + \left(\overline{w'\theta'_v}\right)_{\mathrm{NL}} \tag{1b}$$

with

$$K_h = K_m/\,\mathrm{Pr} + K_{\mathrm{ent}} \tag{2}$$

The nonlocal contribution to the buoyancy flux in equation (1b) arises in convectively active conditions. The basic formulation of this term used in CanaM4 has been retained here for temperature, humidity, and other scalar quantities. It is done in terms of variables that are quasi-conservative and likely to become nearly vertically homogenized in convectively active regions of the boundary layer. This is discussed in detail in section 2.

In principle there could also be nonlocal components of the vertical flux of horizontal momentum. However, this is a vector quantity and horizontal momentum is not a quasi-conserved variable in this context. In particular, accounting for contributions associated with unresolved components of the pressure gradient force presents some conceptual and practical challenges to modeling these nonlocal contributions for the momentum flux vector. This is also an issue in applications of the eddy diffusivity/mass flux (EDMF) approach, which has become popular in recent years to model nonlocal components of turbulent fluxes within the boundary layer (cf. Sušelj et al., 2012). Dealing with these issues is an ongoing topic of investigation. However, we do not attempt to address them in this work.

The first term in equation (2) represents the eddy conductivity associated with turbulence driven by shear production and the local contribution to buoyancy production. The second term represents the effects of entrainment in the capping inversion region of a convectively active boundary layer. The functional forms of the Prandtl number (Pr) and K_{ent} will be defined in section 3 below.

We define the diffusivity for momentum (eddy viscosity for vertical momentum transfer) in terms of the TKE, denoted as k, as

$$K_m = AF_m(Ri)\ell k^{1/2} \tag{3}$$

where the gradient Richardson number (Ri) is defined in such a way as to include the effects of cloudiness and liquid water, as elaborated further in section 7 below.

The structure function $F_m(Ri)$ will be specified such that $F_m(0) = 1$. The definitions of the constant A and the functional form of the master length scale (ℓ) are discussed further below. The usual equation for the TKE is written as (e.g., Lenderink & Holtslag, 2004)

$$\frac{dk}{dt} = -\left(\overline{u'w'}\right)\frac{\partial U}{\partial z} - \left(\overline{v'w'}\right)\frac{\partial V}{\partial z} + \frac{g}{\theta_v}\left(\overline{w'\theta'_v}\right) - T - \varepsilon \tag{4}$$

In this work we ignore the TKE tendency term on the left side of this equation in favor of a quasi-equilibrium formulation in which the main balance is between shear and buoyancy production, dissipation (ε), and turbulent transport (T). The motivation for this is similar to that enunciated by Bretherton and Park (2009). The

turbulence scheme, which includes turbulent transfer within elevated layers in the free atmosphere above the boundary layer, is designed to be used in climate models that typically have effective horizontal spatial resolutions of the order of 100 km or more and utilize time steps that are typically in the range of 10- to 30-min magnitude. The effective temporal resolution associated with such time step magnitudes is usually substantially larger than typical turbulent eddy turnover times within the boundary layer. In practice, TKE budgets on such temporal and spatial scales are often close to a local equilibrium balance between production, dissipation, and transport terms (see Lenderink & Holtslag, 2004).

The transport term is considered to be negligible except within the boundary layer when it is convectively active in association with a positive (upward) buoyancy flux at the surface. These assumptions are similar to those of Bretherton and Park (2009). Details of the formulation of the transport term are presented in section 5 below.

The dissipation term is represented in the usual manner as

$$\varepsilon = k^{3/2}/(B\ell) \tag{5}$$

Note that equations (3) and (5) include the assumption that the mixing length and the dissipation length scale are proportional to each other with both being defined in terms of the master length scale ℓ. In general, this quantity is composed of components from within the boundary layer and the free atmosphere above the boundary layer.

Near the surface the master length scale is constrained to be consistent with classical law of the wall behavior (Mellor, 1989; Mellor & Yamada, 1982) that imposes the constraint that $\ell \propto \kappa z$, where the von Karman constant, κ, has the generally accepted value of 0.4. Within the surface layer turbulent vertical fluxes are assumed to be nearly independent of height. The consistent lower boundary condition for the TKE is

$$k = k_s = c_0 u_*^2 \tag{6}$$

where the friction velocity is defined as $u_*^2 = K_m S$. The magnitude of the wind shear is defined as $S = \sqrt{(\partial U/\partial z)^2 + (\partial V/\partial z)^2}$. The friction velocity is assumed to be nearly independent of height in the surface layer.

We choose $c_0 = 3.75$ and $B = c_0^{3/2}$. As shown below, this correspondence emerges by imposing compatibility between the TKE equation and local similarity theory in the surface layer, as in the works of Baas et al. (2008) and Lenderink and Holtslag (2004).

2.1. Statically Stable Conditions ($Ri > 0$) With Local Equilibrium

We assume that the Prandtl number is close to unity in near neutral conditions but increases with increasing values of the gradient Richardson number. This is consistent with the observational analysis of Mauritsen and Svensson (2007). Using data from several different observational sites, they found that turbulent regimes can be separated into weakly stable, transitional, and strongly stable regimes. Momentum fluxes decrease in magnitude with increasing gradient Richardson number in the transitional regime and become small but finite in the strongly stable regimes. However, the corresponding sensible heat fluxes diminish more rapidly in the transition regimes and may become so small as to be indistinguishable from zero in the strongly stable regimes.

Recent developments in HOC models (Canuto et al., 2008; Zilitinkevich et al., 2007, 2013), as well as LES and direct numerical simulations (DNS) (Venayagamoorthy & Stretch, 2010), suggest that the flux Richardson number (Ri/Pr) approaches a limiting constant value (R_∞) for $Ri \to \infty$. Venayagamoorthy and Stretch (2010) recommend $R_\infty = 0.25$, and this is the default value used in this work. These authors suggest a functional form for the Prandtl number in stable conditions based on DNS results. However, this empirical representation is not directly compatible with the surface layer formulation of Beljaars and Holtslag (1991) that is currently used in the operational CanAM4 model and adapted as discussed below for the present work. Therefore, an alternative representation of the Prandtl number as a function of the gradient Richardson number is developed below to ensure this compatibility.

We consider first a state of quasi-steady, stably stratified local equilibrium where the effect of the transport term on the TKE budget is relatively small and there is a near balance between the shear and buoyancy production and dissipation terms. LES simulations support the assumption that such a balance is a reasonable representative leading approximation in these circumstances. The corresponding approximate TKE equation is given by

$$K_m S^2(1-Ri/\,\mathrm{Pr})-\varepsilon = 0 \tag{7}$$

This gives, with the definitions of eddy viscosity and dissipation rate given above,

$$k = AB\ell^2 F_m^{3/2} \tag{8}$$

$$K_m = A^{3/2}B^{1/2}\ell^2 F_m^{3/2}(1-Ri/\,\mathrm{Pr})^{1/2}S \tag{9}$$

We close these relationships by requiring that $A^3B = 1$. Invoking the lower boundary condition and local similarity in near neutral conditions then gives $A = 1/c_0^{1/2}$ and $B = c_0^{3/2} = 7.26$ as noted above. This definition of the dissipation coefficient is consistent with that of Lenderink and Holtslag (2004) and Baas et al. (2008) when the difference between our definition of the mixing length and theirs is taken into account. They note that their dissipation parameter value is also consistent with the values used in other works that employ the TKE equation with a similar definition of the dissipation rate (e.g., Cuxart et al., 2000) when differing definitions of mixing length scales are taken into account.

It is convenient to define a function $G(Ri, Pr)$ such that

$$G^2 = F_m^{3/2}(1-Ri/\,\mathrm{Pr})^{1/2} \tag{10}$$

so that the quasi-steady equilibrium eddy viscosity and TKE are, with (A, c_0) as defined above, given by

$$K_m = \ell^2 G^2 S \tag{11}$$

$$k = c_0\ell^2 G^{4/3}(1-Ri/\,\mathrm{Pr})^{2/3}S^2 \tag{12}$$

In equation (11) the dissipation length scale plays the role of a neutral stability mixing length. A constraint on G is given by the behavior of the normalized momentum flux (the ratio of the magnitude of the vertical momentum flux vector to the TKE, normalized by its value at $Ri = 0$):

$$\left\langle \frac{|\overline{w'V'}|}{k} \right\rangle = \left(\frac{c_0 K_m S}{k}\right) = \left(\frac{G}{1-Ri/\,\mathrm{Pr}}\right)^{2/3} \tag{13}$$

Data from laboratory experiments, field studies, LES simulations, and recent theoretical studies suggest that this quantity decreases with decreasing shear (increasing gradient Richardson number) in stable stratification but remains finite for large positive values of Ri (Canuto et al., 2008; Ferrero et al., 2011; Kantha & Carniel, 2009; Mauritsen & Svensson, 2007; Zilitinkevich et al., 2008, 2007, 2013). These works suggest the presence of relatively strong mixing regimes for $0 \le Ri \le 0.1$, where the normalized momentum flux is close to its maximum value of unity. However, they also suggest smaller, but finite, limiting values for large values of the gradient Richardson number in turbulent regions above the surface layer.

With these considerations in mind, we account for the dependence of the normalized vertical momentum flux on Ri in a simple empirical way by defining G for stable conditions as

$$G = \left(1-\beta(z)\Gamma^2(3-2\Gamma)\right)(1-Ri/\,\mathrm{Pr}) \tag{14}$$

where $\Gamma = Ri/(R_\infty Pr)$. As noted above and discussed further below, the Prandtl number is defined such that Γ has an asymptotic value of unity for large Ri. The second term in the above expression rapidly approaches its asymptotic value for $Ri > 1$. The functional form of $\beta(z)$ is discussed below in the context of surface layer matching.

2.1.1. Matching to the Surface Layer

In the surface layer, from Monin-Obukhov similarity theory (MOST), diffusivities and vertical gradients of wind, potential temperature, and specific humidity (q) are given by

$$K_m = \left(\frac{\kappa z}{\phi_m}\right)^2 S \quad ; \quad K_h = K_m/\,\mathrm{Pr} = \left(\frac{(\kappa z)^2}{\phi_m \phi_h}\right) S \tag{15}$$

$$K_m S = u_*^2; \quad K_h \partial\theta/\partial z = u_* \theta_* \quad ; \quad K_h \partial q/\partial z = u_* q_* \tag{16}$$

where (u_*, θ_*, q_*) are assumed invariant with height in the surface layer and the dimensionless gradient profile functions ϕ_m,ϕ_h are functions of the variable $\zeta = z/L$, where L is the Monin-Obukhov length $L = \theta_v u_*^3/\left[\kappa g\left(\overline{w'\theta'_v}\right)_s\right]$ with $\left(\overline{w'\theta'_v}\right)_s \cong -u_*\left[\theta_* + .61(\theta_v)_s q_*\right]$.

The use of equations (16) to evaluate surface fluxes in terms of lowest model level prognostic variables is summarized in Appendix 2. In this section we document the formulation of the dimensionless gradient profile functions and matching of the surface layer formulation with that of the remainder of the boundary layer. It follows from equations (15) and (16) that

$$\mathrm{Pr} = \phi_h/\phi_m \tag{17a}$$

$$Ri = \zeta \phi_h/\phi_m^2 \tag{17b}$$

These relationships can be used to express functions of the gradient Richardson number in terms of surface layer variables.

Using the above relationships, the functions Γ and G can written in terms of surface layer variables

$$\Gamma = \frac{1}{R_\infty}\frac{\zeta}{\phi_m} \tag{18}$$

$$G = \left[1 - \beta(z)\Gamma^2(3 - 2\Gamma)\right]\left(1 - \frac{\zeta}{\phi_m}\right) \tag{19}$$

As will be seen below, the effects of transport do not cause a substantial departure from local equilibrium in the surface layer. Therefore, the relevant solutions in that region are given by equations (11) and (12) above. The eddy diffusivity is matched to the surface layer by requiring compatibility between equations (11) and (15), implying that the master length scale in the surface layer has the form:

$$\ell_{\mathrm{sl}} \cong \frac{\kappa z}{\phi_m \mathrm{G}} \tag{20}$$

where, as noted above, G can be expressed in surface layer variables for the purpose of evaluating this *inner* length scale, which will merge with an *outer* scale for the free atmosphere as shown in ((51)) below.

On the stable side ($Ri \geq 0$) in weakly stable conditions, as deduced from analyses of tower observations, $\phi_{m,h} = 1 + \mu\zeta$ with $4 \leq \mu \leq 6$ being the range that seems to fit data reasonably well (Hogstrom, 1996). These empirical formulae are typically valid where ζ does not exceed unity. However, Beljaars and Holtslag (1991) (hereinafter B&H) introduced an extension for more stable conditions under the physically reasonable constraint that the flux Richardson number (Ri/Pr) remains finite and does not exceed the limiting value (R_∞) for large values of Ri. Their extended relationships are

$$\phi_m = 1 + \zeta[a + b(1 + c - d\zeta)\exp(-d\zeta)] \tag{21a}$$

$$\phi_h = 1 + \zeta\left[a\left(1 + \frac{2}{3}a\zeta\right)^{1/2} + b(1 + c - d\zeta)\exp(-d\zeta)\right] \tag{21b}$$

with $a = 1/R_\infty$; $a + b(1 + c) = \mu$. By design these empirical formulae merge with the linear Businger-Dyer (Dyer, 1974) forms for small ζ. In the B&H formulation, $R_\infty = 1$, $d = 0.35$, and $c = 5$ giving $b = 2/3$ for $\mu = 5$. A limiting value less than unity for the flux Richardson number can be made consistent with the B&H formulation if $b = (\mu - 1/R_\infty)/(1 + c)$.

Grachev et al., 2013 have noted that the linear form $\phi_m = 1 + 4\zeta$ is in fair agreement with the Surface Heat Budget of the Arctic Ocean experiment data for turbulent regimes where the flux Richardson number does not exceed.25.

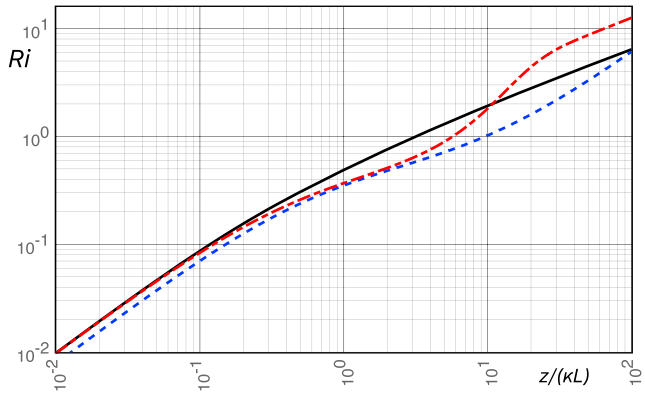

Figure 1. Gradient Richardson number as a function of (z/L), solid curve: as determined from equations (22a) and (22b); red long-short dashed: B&H version as from equations (21a) and (21b); blue dashed: as from equation 82 of Zilitinkevich et al. (2013).

More recently, Li et al. (2015) have derived theoretical expressions for the turbulent Prandtl number for an idealized atmospheric surface layer where scaling does hold for the temperature and vertical velocity spectra. They show that a maximum flux Richardson number exists in these circumstances while the turbulent Prandtl number is a monotonically increasing function of the gradient Richardson number, or alternatively of ζ, in stable conditions.

In light of these observational and theoretical studies, our practical choice is to retain the basic empirical functional forms of the B&H surface formulation currently used in the operational CanAM4 model but modify it for stably stratified conditions to allow for the maximum flux Richardson number to be 0.25. To this end, we take $\mu = 4$ in combination with $R_\infty = 1/4$, in equations (20) leading to $b = 0$ and elimination of the exponential terms. Consequently, with this choice,

$$\phi_m = 1 + 4\zeta \tag{22a}$$

$$\phi_h = 1 + 4\zeta\left(1 + \frac{8}{3}\zeta\right)^{1/2} \tag{22b}$$

The linear behavior of ϕ_m as a function of ζ is the same as equation 70 of Zilitinkevich et al. (2013) and is consistent with experimental data, as noted above, and with LES data as shown in their Figure 10. The nonlinearly increasing behavior of ϕ_h as a function of z/L is a requirement for the absence of a finite critical Richardson number while ensuring that the limiting flux Richardson number is finite and less than unity. The functional form of equation (22b), though adapted from the empirical formulation of B&H, has a qualitatively similar behavior to that of equation 86 of Zilitinkevich et al. (2013), derived using a steady state form of the energy and flux budget model and in good agreement with LES simulation results (see their Figure 11).

The functional forms ((22a) and (22b)) are simple and convenient for use in integral form for determining surface fluxes as outlined in Appendix 2 and for developing a consistent representation of the Prandtl number as a function of the gradient Richardson number as discussed below in section 2.1.2. Figure 1 depicts the gradient Richardson number as a function of $z/(\kappa L)$ for stable conditions corresponding to the B&H equations (21a) and (21b) with $a = 1$ and (22a)s (22a) and (22b), as well as the relationship obtained using the profile functions derived by Zilitinkevich et al. (2013). (Note that their neutral Prandtl number is 0.8). Scaling by the von Karmen constant is introduced to account for the difference between their definition of the Monin-Obukhov length and ours. Their relationship is in good agreement with the LES results depicted in their Figure 12, and the curve for our formulae ((22a) and (22b)) is also in fairly good agreement with the data.

We require that β is positive and becomes asymptotically constant for large $\zeta > 0$. Herinafter, we denote this limiting value as β_∞. In this limit $\Gamma \to 1$. Defining $r = 1/R_\infty - 1$, it follows that, in this limit

$$\phi_m(1 - Ri/\mathrm{Pr}) = \phi_m - \zeta \to r\zeta \tag{23a}$$

$$\phi_m G \to (1 - \beta_\infty) r\zeta \tag{23b}$$

$$\ell_{sl} = \kappa L\zeta/(\phi_m G) \to \kappa L/[(1 - \beta_\infty) r] \tag{23c}$$

Choosing $\beta_\infty = 1 - 1/r$ gives the bounding condition $\ell_{\mathrm{sl}} \le \kappa L$. With $R_\infty = 0.25$ this gives $\beta_\infty = 2/3$. This value provides a reasonably good fit to the published normalized momentum flux data from DNS and LES model results and experimental data (Canuto et al., 2008; Mauritsen & Svensson, 2007).

Cheng et al. (2005) invoke the Nakanishi (2001) formula, derived on the basis of LES simulations for $0 \le z/L \le 0.5$ within the surface layer:

$$\ell_{\mathrm{sl}} \cong \kappa z/(1 + 2.7\zeta) \tag{24}$$

Our formulation, with $R_\infty = .25$, gives the following in the surface layer:

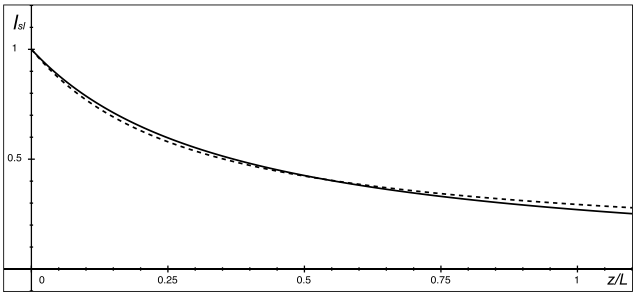

Figure 2. Comparison of equation (25) (dashed) and the Nakanishi (2001) formula (solid) for the normalized surface layer component of the dissipation length scale, $l_{sl} = \ell_{sl}/(\kappa z)$.

$$\ell_{sl} = \kappa z/(1+3\zeta)\left[1-\beta\Gamma^2(3-2\Gamma)\right] \tag{25}$$

Expressing Γ in in terms of ζ, we have found that a close fit of equation (25) to the Nakanishi formula (equation (24)) is achieved by adopting the following functional form for β:

$$\beta = \beta_\infty[\zeta/(1+\zeta)]^2 \tag{26}$$

This gives values that are very close (within 5%) to those for the Nakanishi formulation for $0 \le \zeta \le 0.5$ (Figure 2).

2.1.2. Determining the Prandtl Number as a Function of the Gradient Richardson Number in Stable Conditions

We can now determine the functional form of the Prandtl number as a function of the gradient Richardson number by using equations (21a) and (21b). Substituting those functional forms for the dimensionless profile functions gives the following a fifth-order algebraic equation for z/L, given Ri

$$4\zeta\left[1+4\zeta(1+8\zeta/3)^{1/2}\right]/\left[(1+4\zeta)^2\right] = 4Ri \tag{27}$$

In principle this could be solved explicitly. However, an accurate approximate solution can be obtained more directly by combining asymptotic solutions. For small values of the gradient Richardson number, $\zeta \cong Ri$, while for large values the square-root term dominates giving $\zeta \cong 6Ri^2$. These limiting solutions can be combined to determine a composite approximation as

$$\zeta_e = Ri(1+6Ri) \tag{28}$$

The maximum relative error obtained when this approximate solution is substituted into equation (27) is slightly less than 5.25% of the magnitude of Ri for positive values of the Richardson number.

The resulting approximate Prandtl number for$Ri \ge 0$ is given by

$$\mathrm{Pr} = \left[1+4\zeta_e(1+8\zeta_e/3)^{1/2}\right]/(1+4\zeta_e) \tag{29}$$

where we have assumed a neutral value of unity. As required, this formula has the correct asymptotic behavior for large values of the gradient Richardson number.

As illustrated in Figure 3, the overall behavior of the Prandtl number in stable conditions is in good qualitative agreement with experimental data (Esau & Grachev, 2007) and the DNS results of Venayagamoorthy

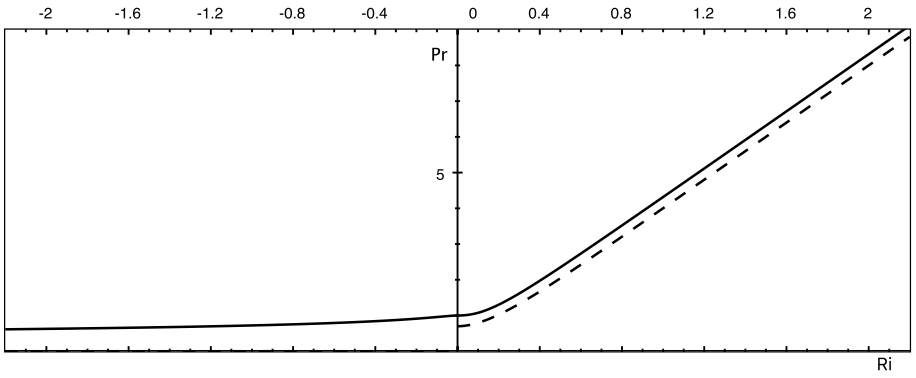

Figure 3. Prandtl number as a function of the gradient Richardson number. Solid: as given by equations (29) and (35). Dashed: as given by the empirical formula of Venayagamoorthy and Stretch (2010) for $Ri \ge 0$ and a neutral Prandtl number of 0.7.

and Stretch (2010) when allowance is made for the fact that we have chosen the neutral Prandtl number to be unity rather than slightly less than unity.

2.2. Statically Unstable Conditions ($Ri < 0, \zeta < 0$)

In weak to moderately unstable conditions we adopt the most commonly used empirically derived flux profile relations of the form

$$\phi_m = (1-\gamma_m\zeta)^{-1/4};\ \ \phi_h = (1-\gamma_h\zeta)^{-1/2} \tag{30}$$

where $\zeta = z/L \leq 0$.

Published empirical profile functions derived from analyses of field data show a wide range of values for the parameters in these formulae (Hogstrom, 1988, 1996) but the values typically used currently for γ_m are in the range $15 \leq \gamma_m \leq 20$ (cf. Hogstrom, 1996). Consistent with the foregoing we set the neutral Prandtl number to unity. Continuity of ϕ_m with the functional form (22a) on the stable side at $\zeta = 0$ suggests $\gamma_m = 16$, which is within the above range for the values.

Using these relations gives the following expression for the Prandtl number:

$$\mathrm{Pr} = \frac{\phi_h}{\phi_m} = \frac{(1-\gamma_m\zeta)^{1/4}}{(1-\gamma_h\zeta)^{1/2}} \tag{31}$$

Continuity of the slope of the Prandtl number with the stable side at $\zeta = 0$ requires that $\partial\, Pr\, /\partial\zeta = 0$ at that point and therefore that $\gamma_h = \gamma_m/2$. With $\gamma_m = 16,\ \ \gamma_h = 8$, this gives values for ϕ_m and ϕ_h that are within the range of published results in the range $-1 \leq \zeta \leq 0$ (e.g., Figures 3 and 4 of Hogstrom, 1996). These choices are also close to those used in the current operational CanAM4 surface flux formulation ($\gamma_m = 15, \gamma_h = 9$).

The relationship between ζ and the gradient Richardson number is given by

$$\zeta\left(\frac{1-\gamma_m\zeta}{1-\gamma_h\zeta}\right)^{1/2} = Ri \tag{32}$$

The terms involving ζ dominate in the square-root factor for modest and large magnitudes of ζ indicating that in this limit

$$Ri \cong \left(\frac{\gamma_m}{\gamma_h}\zeta^2\right)^{1/2} = \sqrt{2}\zeta \tag{33}$$

This is in reasonable agreement with the relationship $Ri = 1.5z/L$ suggested by Hogstrom 1996.

Equation (32) can be written as a cubic equation to determine ζ in terms of Ri. However, an accurate approximation (errors less than 2% of the magnitude of Ri) that satisfies the appropriate limits for small and large negative values of the Richardson number is given by

$$\zeta \cong \zeta_* = Ri\left(\frac{1-\gamma_h Ri}{1-\gamma_m Ri}\right)^{1/2} \tag{34}$$

The resulting approximate Prandtl number is given by

$$\mathrm{Pr} = \frac{(1-\gamma_m\zeta_*)^{1/4}}{(1-\gamma_h\zeta_*)^{1/2}} \tag{35}$$

This expression does not impose a lower bound on the Prandtl number. Cuxart et al. (2000) and Lenderink and Holtslag (2004) suggest that, in practice, the inverse Prandtl number should not exceed 2 in unstably stratified conditions. This is in fact the case for the above expression for the usual range of negative Richardson numbers that are encountered (Figure 3).

As discussed below, we utilize the free-convective extension to the Monin-Obukhov formulation proposed by Beljaars (1994) as documented by Abdella and McFarlane (1996). However, this has little effect on diffusive component of the scalar fluxes in these circumstances as they are maintained in a near neutral state above the surface layer by the nonlocal component of the flux profile discussed below.

In these circumstances the lower part of the surface layer itself is the only region where the Richardson number is significantly negative within the boundary layer. We will simply impose as a limiting behavior that $G\phi_m \to 1$ in the formal limit of z/L being large and negative within the surface layer. In the absence of explicit free-convective effects, this ensures that $\ell_{sl} \to \kappa z$ in this limit. As outlined below, a free-convective enhancement of ℓ_{sl} will be introduced but it is assumed that it does not affect this constraint on the functional form for G. A simple formulation for G for $Ri < 0$, defined in a way that merges with the stable side formulation and with this limiting condition, is as follows:

$$G = 1 - \frac{Ri}{\mathrm{Pr}\left[1 - (\gamma_h/\gamma_m)^{1/2} Ri\right]} \tag{36}$$

Using the surface layer representations of the relevant variables, on the unstable side, note that

$$G_{SL}\phi_m = \phi_m - \frac{\zeta}{1 - \zeta(\gamma_h/\gamma_m)^{1/2}\phi_h/\phi_m^2} \tag{37}$$

This approaches unity when z/L is large and negative while L is finite. The corresponding form for ℓ_{sl}, in the absence of explicit free-convective effects, is given by

$$\ell_{sl} = \frac{\kappa z}{\phi_m G_{SL}} = \frac{\kappa z}{\left(\phi_m - \frac{\zeta}{f}\right)} \;\; ; \;\; f = 1 - \zeta(\gamma_h/\gamma_m)^{1/2}\phi_h/\phi_m^2 \tag{38}$$

2.2.1. Free Convection and Nonlocal Mixing

The Monin-Obukhov theory becomes formally singular in the limit $u_* \to 0; L \to 0$ as would be the case for purely buoyant convection. In the present work this is circumvented by including the free convection modification proposed by Beljaars (1994) wherein the effective mean wind speed that is used in the surface layer formulation is that at the lowest model level plus a free convection enhancement proportional to the convective velocity scale, such that $|U^2|_{\mathrm{eff}} = |U^2| + b_{fc} w_*^2$, where b_{fc} is an empirical constant whose value is of the order of unity (currently has the default value of 1.2). Since the convective velocity scale depends on the effective wind speed, this formulation is implemented through an iterative procedure in the surface layer formulation of Abdella and McFarlane (1996) that is also used in the present work.

However, even when wind speeds are finite in the near surface region of convectively active boundary layers, such as that occur in cloud-free boundary layers over relatively warm surfaces in the daytime, upward heat and buoyancy fluxes occur throughout most of the boundary layer, typically with mixing effects that are sufficiently strong to maintain the thermal stratification of the boundary near neutral through most of the boundary layer. The statically unstable *constant flux* surface layer typically occupies a thin layer whose depth is only a few percent of the depth of the boundary layer (Zilitinkevich et al., 2006).

Therefore, in practice, negative gradient Richardson numbers are likely to be a rare occurrence above the surface layer and most likely in circumstances of very weak mean horizontal winds accompanied by episodic gusts associated with the occasional presence of deeper eddies that are not resolved in large-scale models. In these circumstances the local down-gradient diffusive heat flux formulation discussed above cannot sustain upward heat and buoyancy fluxes in the presence of neutral (or even slightly stable) stratification in the boundary layer.

However, it is now well established that fluxes of scalar quantities in such convectively active regimes, associated with buoyant eddies that occupy most of the depth of the well-mixed part of the boundary layer, are substantially nonlocal in nature. The vertical flux of a quasi-conserved scalar variable χ can be represented as the sum of local diffusive contributions and nonlocal, nondiffusive contributions:

$$\left(\overline{w'\chi'}\right) = -K_\chi \frac{\partial \overline{\chi}}{\partial x} + \left(w'\chi'\right)_{NL} \tag{39}$$

Higher moment closure models treat the nonlocal effects as combinations of third moments of turbulent quantities, predominantly vertical velocities, and quasi-conserved scalar variables. There is a large literature and long history of nonlocal formulations based on higher moment closure as discussed in detail by Cheng et al., 2005 and more recently by Canuto et al., 2007 who also include a discussion of plume-based formulations for higher moments. Plume-like representations of higher moments have also been explored in other works (see also Abdella & McFarlane, 1996, 2001; Lappen and Randall, 2001; Larsen and Golaz, 2005).

Recently, adaptations of the EDMF formulation proposed by Siebesma et al. (2007) have been adopted by a number of modeling groups. This formulation accounts for nonlocal contributions to vertical fluxes of quasi-conserved scalar variables in convectively active boundary layers in terms of a bulk mass flux formulation. While the EDMF formulation appears to perform well and has appealing practical features, we have chosen herein to retain and adapt the relaxational nonlocal mixing formulation used in the current operational CanAM4 model (von Salzen et al., 2013). This scheme essentially emulates bulk mixed layer effects in a multilevel context.

In circumstances where enhanced nonlocal effects are important it is assumed that the well-mixed region of the boundary layer extends down to the lowest model layer and evolves in such a way that, within a region of depth h_* adjacent to the surface and just below a capping inversion in the virtual potential temperature profile, quasi conserved scalar variables (such as potential temperature and specific humidity in a dry cloud-free boundary layer) become nearly homogeneous in the vertical in association with a nearly linear decrease of the buoyancy flux with height to zero at the top of this region. It is assumed that the nonlocal components of the turbulent fluxes for all of the scalar variables are also zero at this level. We bypass the details of the nonlocal processes and instead assume that their net effect is to relax scalar variables to these vertically homogeneous states such that

$$\left(\frac{\partial \overline{\chi}}{\partial t}\right)_{\mathrm{NL}} = \frac{1}{\tau_m}\left(\chi_R - \overline{\chi}\right) = -\frac{1}{\overline{\rho}}\frac{\partial}{\partial z}\left[\overline{\rho}\left(\overline{w'\chi'}\right)_{\mathrm{NL}}\right] \tag{40}$$

Here the reference vertically homogenized variable χ_R is independent of height. The relaxation timescale, τ_m is specified below. We specify the reference value as

$$\chi_R = \langle \overline{\chi} \rangle + a_\chi \frac{\left(\overline{w'\chi'}\right)_s}{\left(\sigma_w\right)_s} \tag{41}$$

where

$$\langle \overline{\chi} \rangle = \frac{\int_0^{h_*} (\overline{\rho\chi}) \mathrm{d}z}{\int_0^{h_*} \overline{\rho} \mathrm{d}z} \tag{42}$$

and a_χ is a specified fraction of the surface flux and $(\sigma_w)_s$ is the vertical velocity variance in the surface layer associated with turbulent motions.

We have adapted an empirical formula proposed by Holtslag and Moeng (1991) based on LES results to express the vertical velocity variance as

$$\left(\sigma_w\right)_s = 1.3\left(u_*^3 + 0.6\frac{z_1}{h}w_*^3\right)^{1/3} \tag{43}$$

where z_1 is the height of the lowest model level above the local surface. Note that, in the convective limit, such that $w_* \gg u_*$, (41) and (43) are consistent with the form expected at the lowest model level for classical free convective conditions (cf. Zilitinkevich et al., 2006).

Consistent with the above assumptions we may define the associated nonlocal flux at any level within this region as

$$\left(\overline{w'\chi'}\right)_{\mathrm{NL}} = \frac{1}{\bar{\rho}\tau_m}\int_z^{h_*} \overline{\rho(z)}\left(\chi_R - \overline{\chi}(z')\right)\mathrm{d}z' \tag{44}$$

At the surface this quantity is equal to the specified fraction a_χ of the surface flux. The contributions from the mean state integrates to zero in this limit so that this requirement then sets the relaxation timescale as

$$\tau_m = \frac{1}{(\sigma_w)_s}\int_0^{h_*} \frac{\bar{\rho}}{\bar{\rho}_s}\mathrm{d}z \tag{45}$$

This is in the form of an eddy turnover timescale for the mixed layer.

The default value of unity for the fraction a_χ is used in the current operational version of CanAM4. We have retained this default value for the current implementation. In practice it has been found to produce realistic boundary layer structures for the typical configuration of levels and time-step length used in the GCM. In this case, the mixing associated with the nonlocal process is efficient in producing vertically homogeneous profiles of scalar prognostic variables within the mixed region. Consequently, fluxes of heat, moisture, and other scalar prognostic variables are entirely accounted for in terms of the nonlocal contribution. In these circumstances the well-mixed part of the boundary layer evolves in a way that is similar to that of a bulk mixed layer, at least in respect of scalar prognostic variables.

The quantity h_* is not known a priori. It is assumed to coincide with the upper interface of the lowest model level such that the virtual potential temperature for the reference state is less than the mean value in the layer above but equal to or larger than all values of the mean virtual potential temperature in the region below this level, that is, $\overline{\theta}_v(h_* + \delta z/2) > (\theta_v)_R > \overline{\theta}_v(z)$ for $z \le h_*$. This level is determined iteratively by strapping layers together, starting from the two lowest layers, and evaluating reference variables until a level is reached such that this condition is satisfied. When this level is found the corresponding relaxation timescale is defined.

In the operational CanAM4 model the nonlocal scheme is applied whenever the buoyancy flux at the surface becomes positive (upward). In practice situations can arise where surface buoyancy fluxes, though positive, are small in magnitude and possibly fluctuating from one time step to the next. This can happen in morning hours in clear-sky conditions where surface sensible heat fluxes are undergoing a transition from downward to upward in response to surface heating. Through experimentation with the SCM we have concluded that it is preferable to leave the nonlocal mixing inactive until upward surface buoyancy flux regimes become established and persistent. We do this in a simple way by defining triggering and cessation conditions for the nonlocal mixing in terms of the history of the surface buoyancy flux. We define a temporally filtered buoyancy flux, $\widehat{Q}_s$, as follows

$$\partial\widehat{Q}_s/\partial t = \frac{1}{\tau_a}\left(\left(\overline{w'\theta'_v}\right)_s - \widehat{Q}_s\right) \tag{46}$$

where the filter timescale τ_a is chosen empirically to damp fluctuations with periods shorter than a specified number of model time steps.

For the TKE scheme, the nonlocal mixing scheme is invoked only when both the buoyancy flux at the surface and the filtered value are positive (upward). The introduction of positivity of $\widehat{Q}_s$ as an ad hoc triggering condition ensures that upward buoyancy fluxes have become persistent as a condition for the nonlocal mixing scheme to operate efficiently. We have not found strong sensitivity to varying the filter timescale from 15 to 60 min in SCM simulations using a time step of 5 min. The results shown in section 8 below were obtained with $\tau_a = 60$ min for the TKE scheme.

As for the current operational implementation in CanAM4, the nonlocal mixing scheme is not applied within cloudy regions in the boundary layer. Although, in the absence of precipitation, quasi-conserved variables can exhibit nearly well mixed structures within cloudy regions, the nonlocal mixing is

confined to levels below cloud base in regions where cloud develops within a convectively active boundary layer. This constraint is imposed to avoid interference between this scheme and the separately activated moist convection schemes. Currently, these schemes are as described in the von Salzen et al. (2013) paper and references therein. At this point the TKE and operational moist convection parameterization schemes are not explicitly coupled. Work on this topic is under way but is beyond the scope of the present study.

The nonlocal mixing process is not applied to momentum for the reasons noted in section 1. To our knowledge, our practice of applying it only to scalar prognostic variables is similar to that in most current implementations of the EDMF scheme. However, the surface-based component of the master length scale for convectively active conditions is adjusted by including a convective factor such that equation (38) is replaced by

$$\ell_{\rm sl} = \frac{\kappa z}{\phi_m - \zeta/(f_c f)} \quad ; \quad f_c = \left(1 - \nu_{fc}\zeta\right)^{1/3} \tag{47}$$

We currently use $\nu_{fc} = 8$. This formulation effectively allows an enhancement of the eddy viscosity to emerge in convectively active conditions.

3. Master Length Scale in the Boundary Layer Above the Surface Layer and the Free Atmosphere

A traditional definition of the master length scale is the Blackadar inverse interpolation form, adapted for the formulation of the surface layer, defined as

$$\frac{1}{\ell} = \frac{1}{\ell_{\rm sl}} + \frac{1}{\ell_\infty} \tag{48}$$

where $\ell_{\rm sl}$ is the inner length scale as defined and discussed above and ℓ_∞ is an outer length scale specified independently. The inverse interpolation in equation (51) then ensures that the magnitude of the master length scale does not exceed that of the smaller of these component scales. We have adopted this approach to defining the master length scale within the boundary layer.

It has become a common practice in boundary layer modeling to set the outer length scale to be equal to a specified small fraction of the depth of the boundary layer (cf. Bretherton & Park, 2009). However, it can also be defined so that it exceeds this value within the well-mixed part of the boundary layer (Lenderink & Holtslag, 2004).

However, stable stratification acts to limit the vertical depth of turbulent eddies. In such conditions a commonly invoked constraint in atmospheric modeling is to limit the dissipation length scale by a length scale that is proportional to $k^{1/2}/N$ (where N is the buoyancy frequency), as suggested by Deardorff (1980) who took the proportionality constant to be 0.76. However, Schumann (1991) noted that this particular value has no formal justification and in fact could be much smaller due to effects of anisotropy.

It is noteworthy that the limiting length scale as defined above is related to the Ozmidov scale, defined as $\ell_0 = (\varepsilon/N^3)^{1/2}$. Using the definition of the dissipation rate given in equation (5), with $c_0 = B^{2/3}$, the Ozmidov scale can be written as

$$\ell_0 = \ell\left(\frac{k^{1/2}}{c_0^{1/2} N \ell}\right)^{3/2} \tag{49}$$

Therefore, the condition $\ell \le k^{1/2}/\left(c_0^{1/2} N\right)$ also ensures that the Ozmidov length scale exceeds the dissipation length scale. In homogeneous stably stratified turbulence theory the Ozmidov scale characterizes the size of the larger eddies in the inertial subrange that is associated with the down-scale kinetic energy cascade that culminates in the Kolmogorov scale where kinetic energy dissipation acts (cf. Schumann, 1991).

We define a limiting dissipation length scale for stable stratification as $\ell_{\lim} = \text{const}(k^{1/2}/N)$. Then, under local equilibrium as defined by equation (12)

$$\ell_{\lim} = \text{const}\left(c_0^{1/2}\right)\ell/Y^{1/2};\;\; Y = Ri/\left[G^{4/3}(1-Ri/\,\text{Pr})^{2/3}\right]; Ri > 0 \tag{50}$$

The quantity Y is a function of the background state and therefore may take on a range of positive values in stable stratification. We choose const $= 1/c_0^{1/2} \cong 0.517$. This is within the range of values that have been used in the literature as discussed above, is consistent with the limiting scale being bounded by the Ozmidov scale, and is a convenient choice as it gives $\ell_{\lim} \geq 1$ if $Y \leq 1$.

Baas et al. (2008) used a similar limiting length scale for the mixing length, specified as $\ell_h = c_h k^{1/2}/N$ in a TKE formulation similar to that of Lenderink and Holtslag (2004). Using a linear form for the functional relationship between the Prandtl number and the Richardson number, they derived a condition, conceptually equivalent to $Y = 1$, for the existence of real and finite values of the TKE. However, they interpreted it as imposing a condition on the ratio Ri/Pr to ensure compatibility with local equilibrium under these constraints. Applying this interpretation in the surface layer determines limiting values of the ratio ζ/ϕ_m that are compatible with local equilibrium and the mixing length definition. They found that physically acceptable real valued equilibrium solutions only exist for certain combinations of the constants c_h, c_0, and R_∞. These solutions are all associated with linear forms for the dimensionless profile functions with associated finite critical Richardson numbers.

As discussed in section 2.1 above, we have chosen the forms of the functions ϕ_m, ϕ_h to avoid imposing a finite critical Richardson number in the surface layer. The dissipation length scale for the surface layer is consistently defined through the matching condition (20) and is limited by the Monin-Obukhov length in stable conditions. Therefore, the limiting length scale constraint is applied only to the outer length scale.

Above the surface layer, turbulent mixing in the boundary layer, particularly during convectively active periods in the daytime, typically ensures that Y is less than unity in that region. However, it increases rapidly with height in the free atmosphere above the boundary layer. Imposing the limiting length scale in this region is not consistent with steady equilibrium with finite values of the TKE if $Y > 1$. However, LES results do not support an abrupt cessation of turbulence at a finite gradient Richardson number for stably stratified quasi-steady conditions (Kosovic & Curry, 2000; Mirocha & Kosovic, 2010).

This issue has been discussed by Cheng et al. (2004). They suggest that the limiting length scale can be evaluated using the TKE defined for a reference length scale that would apply in the absence of a limitation. They used the outer length scale defined by Mellor and Yamada (1974) as a reference scale. The TKE is then evaluated using the smaller of this limiting length scale and the reference length scale.

To apply this concept, we consider the regions within and above the boundary layer separately. Within the boundary layer, we define the outer length scale as follows:

$$\ell_\infty = \max\left[(\ell_{\text{sl}}(h) - \ell_{\text{sl}}(z) + \eta h)/\max\left(Y(z)^{1/2}, 1\right), \ell_{\min}\right]; z \leq h \tag{51}$$

The parameter η is assigned the default value of 0.15 but may be adjustable in the range (.075, 0.15) as suggested by LES simulations (e.g., Bretherton and Park (2009)), and $\ell_{\min}$ is a specified minimum value imposed for practical numerical reasons. In the present work, the default value for this quantity is 10 m.

Above the boundary layer, for the current quasi-steady equilibrium version, we take the reference length scale to be the value of the length scale at the level below, which has been previously determined by marching upward level by level. In this case the master length scale at any level based on its value at the level below is as follows

$$\ell(z_j) = \max\left[\min\left(k^{1/2}(z_j; \ell(z_{j-1}))/\left(c_0^{1/2}N_j\right), \ell(z_{j-1})\right), \ell_{\min}\right] \tag{52}$$

where the subscript j denotes the level index, increasing upward from the bottom, and $k(z_j; \ell(z_{j-1}))$ is an

estimate of the TKE at level j, determined using the dissipation length from the level below. When local equilibrium applies this gives

$$\ell(z_j) = \max\left(\frac{\ell(z_{j-1})}{\max\left(Y_j^{1/2}, 1\right)}, \ell_{\min}\right) \tag{53}$$

As noted above, $Y(z)$ increases with rapid height in the capping inversion and the stratified free atmosphere above the boundary layer where it typically exceeds unity. Thus, under local equilibrium, the above definition of the length scale ensures that the master length scale decreases with height in this region until reaching $\ell_{\min}$ in the absence of additional forcing or turbulence generation mechanisms, such as internal gravity-wave breaking.

Within the boundary layer ℓ_∞ increases downward, resulting in a maximizing of ℓ within the boundary layer. This formulation is conceptually equivalent to the ($\ell_{\text{up}}, \ell_{\text{down}}$) formulation that is used in the operational CanAM4 boundary layer scheme and in a number of other previously published studies (e.g., Lenderink and Holtslag (2004)).

4. Determining the Top of the Boundary Layer

We have implemented a version of the bulk Richardson number criterion suggested recently by Richardson et al. (2013) to determine the vertical extent of the boundary layer for conditions in which the surface layer is stable (downward buoyancy flux at the surface) as well as unstable, such that it includes at least part of the stably stratified capping region above the well-mixed part of the convectively active boundary layer. The boundary layer is defined as the region adjacent to the surface where the bulk Richardson number for the boundary layer is less than a critical value that depends on z/L when that quantity is positive.

The bulk Richardson number for the boundary layer is defined as

$$R_i^{(b)} = \frac{gh}{\overline{\theta}_v^{(s)}} \frac{\overline{\theta}_v - \overline{\theta}_v^{(s)}}{\left|\overrightarrow{\overline{V}(z)}\right|^2} \tag{54}$$

where $\overrightarrow{\overline{V}}$ is the local large-scale mean horizontal wind vector and $\overline{\theta}_v^{(s)}$ is the potential temperature at the surface. The top of the boundary layer is defined as the highest level such that $R_i^{(b)} \leq \max(\nu_{bl} z/L, 1)$ for $z \leq h$. Here we take $\nu_{\text{bl}} = 0.045$ as suggested by Richardson et al. (2013). This definition ensures that the boundary layer includes the well-mixed part in a convectively active boundary layer as well as part of the stably stratified capping layer above it.

5. TKE Transport

Traditionally, the TKE transport term is represented using a diffusive approach. However, such an approach has some limitations in convectively active boundary layers where vertical gradients of the TKE can become small and nonlocal effects associated with organized deep updrafts play a major role in the transport process (cf. Witek et al., 2011). As noted above, we have adopted an empirical formulation similar to that proposed by Bretherton and Park (2009, hereinafter B&P) for the transport term. Consistent with results of LES simulations, it is assumed that the vertical transport is predominantly confined to the atmospheric boundary layer in convectively active conditions when the buoyancy flux in the surface layer is positive (upward). It is further assumed that the vertical mixing effect of the transport term is to relax the TKE to a vertically homogeneous state on a timescale that is proportional to the local turbulent eddy turnover time:

$$T = -\frac{\alpha k^{1/2}}{\ell}(k_* - k) \tag{55}$$

The quantity k_* is vertically constant and should be chosen so that the vertically integrated transport vanishes.

Here α is dimensionless and in principle a function of height above the surface. B&P take it to be unity in the convectively active part of the boundary layer and zero otherwise. However, since $\ell \propto \kappa z$ in the surface layer, boundedness of the transport term at the surface, as is required for consistency with the lower boundary condition for the TKE (Mellor, 1989), can only be ensured if $\alpha(0) = 0$. Therefore, we define a functional form for $\alpha(z)$ so as to ensure that it is nonzero within a convectively active boundary layer and a narrow flanking region immediately above the top of the boundary layer.

To achieve this behavior in a simple but adjustable way we define α in terms

of the variable $Z_\alpha = z/h$ as follows:

$$\alpha(z) = \alpha_{\max} \nu_{\mathrm{tr}} Z_\alpha \exp(1 - \nu_{\mathrm{tr}} Z_\alpha); \quad 0 \le Z_\alpha < 1/\nu_{\mathrm{tr}} \tag{56a}$$

$$\alpha(z) = \alpha_{\max}; 1/\nu_{\mathrm{tr}} \le Z_\alpha \le 1 \tag{56b}$$

$$\alpha(z) = \alpha_{\max} Z_\alpha \exp\left[1 - Z_\alpha - \left(\max\left(\frac{z-h}{d}, 0\right)\right)^2\right]; \quad Z_\alpha > 1 \tag{56c}$$

The enhanced damping above the boundary layer is introduced to ensure that the effects of transport are predominantly confined to the boundary layer and a narrow flanking region above it. The parameter $\nu_{\mathrm{tr}} > 1$ allows the region where α increases with height to be confined to a fraction of the depth of the boundary layer. Clearly, the choice of unity for this fraction merges the three subregions into one, defined by equation (56c).

We define a convectively active boundary layer as existing when the surface sensible heat flux is positive (upward). The transport and entrainment processes are activated in these circumstances if the boundary layer, as determined by invoking the bulk Richardson number procedure outlined above, is at least three model layers deep.

We currently choose $\alpha_{\max} = 1$, $d = 10$ m, and $\nu_{\mathrm{tr}} = 6$. It should be noted that the parameter choices are made empirically and depend to some extent on the vertical resolution of the model. We require that the depth of the region where α increases with height is at least as large as that of the lowest model layer.

Under sufficiently strongly convectively active conditions, the boundary layer would typically be deep enough so that $\alpha = \alpha_{\max}$ throughout most of the well-mixed portion. In these circumstances the effective relaxation timescale in the well-mixed part of the boundary layer would be the local eddy turnover timescale as in the B&P formulation. The combined effects of the TKE transfer process and nonlocal heat and moisture transfer (discussed above) would act to homogenize the TKE throughout well-mixed portion of the boundary layer. The function α is also used to modulate the entrainment term as discussed below.

5.1. Determining k_*

We determine k_* so that the (mass-weighted) vertical integral of the transport term is zero:

$$\int_0^\infty \frac{\overline{\rho}}{\overline{\rho}(0)} \alpha(z) \left(\frac{k}{\ell^2}\right)^{1/2} (k_* - k) \mathrm{d}z = 0 \tag{57}$$

The integrand is seen to be a nonlinear function of k_* through the functional dependence of k on k_*. Consequently, satisfying this constraint is coupled to solving the full TKE equation. This is discussed in Appendix 1.

6. Entrainment

The local form of the eddy conductivity, $K_h = K_m/Pr$, does not adequately account for the effects of buoyancy-driven entrainment at the top of the boundary layer in convectively active conditions accompanied by weak wind shear. In part this is because the gradient Richardson number becomes large in the presence of stable stratification and weak shear with the result that the Prandtl number also becomes large. To rectify this situation, the additional entrainment that is needed is modeled by introducing the quantity K_{ent}

that is assumed to be nonzero only in the stably stratified transition layer that includes the capping inversion. Otte and Wyngaard (2001) suggest that

$$K_h \sim \sigma_w^2 / N \tag{58}$$

in the entrainment layer with a proportionality factor of.2–.3, where they also conclude from their data that the vertical velocity variance is given approximately by $\sigma_w^2 \cong .16k$. Following this guidance K_{ent} is assumed to be of the form

$$K_{\text{ent}} = \Lambda k / N \;\; ; N > 0 \tag{59}$$

Entrainment is closely linked to the effects of penetration of deep eddies into the capping inversion at the top of the convectively active boundary layer. These same eddies are responsible for the TKE transport within the convectively active boundary layer, as suggested by Otte and Wyngaard (2001). With this consideration in mind we assume that these two processes are both controlled in part by the profile function $\alpha(z)$ defined above. To that end, and for notational convenience in the kinetic energy budget (see Appendix 1), we define $\Lambda = \Lambda_* \alpha / c_0^{3/2}$. We have chosen $\Lambda_* = .35$ as the default value for simulations of the diurnal evolution of a cloud-free convectively active daytime boundary layer.

7. Modifications for Cloudy Conditions

The operational treatment of stratiform clouds used in CanAM4 is retained within the TKE scheme. The effects of clouds on heat, moisture, and buoyancy fluxes are taken into account using formulations that are similar to Lenderink and Holtslag (2004) and Bretherton and Park (2009). In particular, the Brunt-Vaisala frequency is defined in terms of gradients of the quasi-conserved variables total water and liquid water static energy as

$$N^2 = [C_s A_m + (1 - C_s) A_d] \frac{\partial s_l}{\partial z} + [C_s B_m + (1 - C_s) B_d] \frac{\partial q_t}{\partial z} \tag{60}$$

where C_s is the local fractional cloud area at a given level and the total water and condensed water static energy are defined as

$$q_t = q_v + q_w + q_i \tag{61a}$$

$$s_l = c_p T + gz - L_v q_w - (L_v + L_f) q_i \tag{61b}$$

or, in combination, as the more traditional moist static energy

$$h = s_l + L_v q_t + L_f q_i = c_p T + L_v q_v + gz \tag{61c}$$

The coefficients ($A_{m,d}$,$B_{m,d}$) are adapted from separate formulae for cloud free and cloud covered conditions following Schubert et al. (1979).

We have also included an optional evaporative enhancement of the entrainment at the top of a cloud-topped boundary layer. The enhancement factor is defined in a manner similar to that of Bretherton and Park (2009), as follows:

$$K_{\text{ent}} = (K_{\text{ent}})_d \left[1 + \alpha_{\text{evp}} (0.8 L_v q_l / \Delta s_v)\right] \tag{62}$$

where $(K_{\text{ent}})_d$ is the entrainment diffusivity at the upper interface of a layer in the absence of cloud in the layer, as defined in equation (62), and Δs_v is the difference in the virtual static energy between the midpoints of the layer above and the cloudy layer. This enhancement is currently invoked at the upper interface of a cloudy layer within the entrainment region if Δs_v is positive and the layer above it is cloud free. We assume that the evaporative coefficient is adjustable to some extent. Bretherton and Park (2009) suggest that $10 \le \alpha_{\text{evp}} \le 30$. We currently use $\alpha_{\text{evp}} = 30$ as the default value.

8. Testing With the CanAM SCM

8.1. The SCM

The SCM used here is based on the column physical processes package of the CanAM4 model as documented in von Salzen et al. (2013). It operates as a stand-alone SCM through a separate driver that has been adapted and modified for the work presented herein. The complete CanAM4 column physical processes package includes the operational modules for land surface processes, radiative transfer, stratiform clouds and aerosol parameterizations, shallow and deep cumulus parameterizations, gravity-wave drag, and turbulent transfer parameterizations. Not all of these modules are used in the current work. The operational CanAM4 turbulent transfer scheme and the new TKE scheme are used interchangeably and compared in the results presented below. The radiative transfer module has been included in all cases unless otherwise specified, and the stratiform cloud scheme was included for cloudy cases. For the cases considered below the gravity-wave drag and the cumulus parameterization modules have been deactivated for the present work.

The pressure-based hybrid vertical coordinate used in CanAM4 is retained in the SCM. The grid spacing utilized is typically also the same as that in the corresponding version of CanAM4. There are currently two versions of this configuration available, one being the 49-level operational configuration and the other being an experimental 53-level configuration with enhanced vertical resolution near the surface. This version nominally has 11 levels within the lowest 800 m at heights of approximately 8.9, 17.9, 35.8, 62.8, 107.9, 171.2, 243.9, 381.1, 510.7, 641.5, and 773.8 m. By comparison, the operational 49-level version has 7 levels in this range located approximately at 40.1, 112.8, 227.2, 343.3, 461, 580.6, and 701.9 m.

The 53-level version is used for the work reported herein. It is important to note that simulations with the operational scheme made use of the operational implementation as documented in von Salzen et al. (2013) with a single modification for the 53-level SCM simulations to restrict application of the imposed 10-m minimum mixing length to levels that are higher than 40 m above the surface. A minimum background diffusivity of 0.1 $m^2/_s$ in the free atmosphere above the boundary layer has been retained for both the operational and TKE schemes.

The simulation for the Dynamics and Chemistry of Marine Stratocumulus (DYCOMS) case study presented in section 8.3 below was carried out to illustrate the performance of the TKE scheme in a marine boundary layer stratocumulus regime where the interaction of turbulence and cloud processes is important.

8.2. Simulations of the Clear-Sky Diurnal Cycle—Comparison With Cabauw Observations

The Cabauw, Netherlands tower (51.971 N, 4.927°E) provides continuous observations of temperature and wind at 2, 10, 20, 40, 80, 140, and 200 m and cloud frequency and cloud base information from ceilometer backscatter data. The study period chosen for this work is during the summer months (June-July-August) of the 5-year period from January 2007 to December 2011. Observations from the Cabauw Observatory for 1–2 July 2006 were used for the Third GABLS Intercomparison case study (Bosveld et al., 2014). Although the data used here is from a later and much longer period of observations at the Cabauw Observatory, and our emphasis is on the simulating climatological features, our simulations address the same modeling issues as were addressed in the Third Global Energy and Water Exchanges (GEWEX) Atmospheric Boundary Layer Study (GABLS) Intercomparison study.

Since the focus of the present study is primarily on the boundary layer turbulence scheme we confine attention to comparison with the Cabauw tower observations in predominantly clear-sky conditions. In these circumstances the diurnal evolution of the boundary layer is likely to be predominantly affected by local conditions, while in cloudy regimes there may be a number of additional factors, including synoptic-scale activity and moist convection that affect cloud cover, precipitation, and boundary layer structure in ways that have not been explicitly represented in the SCM simulations carried out for this study.

Mean statistics for clear-sky regimes have been compiled from the observational data from the Cabauw site (He et al., 2012) and are used here to compare with model results. Clear-sky days are selected as days in which there are at least 18 hr, including the periods between local sunrise and sunset, where there are at least 4 periods of 10 min during each hour when no cloud is reported.

For simulations over land surfaces, the SCM includes the most recent operational (CLASS 3.6) version of the CanAM soil and land surface scheme. Surface fluxes, surface, and soil temperatures are fully coupled with

the land surface scheme. During the first 10 days of each simulation the ground surface temperature is maintained at observed values. Surface and soil properties are set to those of the closest land surface AGCM grid box to the Cabauw site with a surface roughness of 0.1 m. The soil moisture profile is specified with volumetric liquid water content set to 0.20 m3/m3. The land surface type is set as open grass (type 4), with soil structure (first and second layers: clay:5%, sand 5%, organic matter (ORGM) 30%; third layer: clay: 40%, sand: 0%, ORGM 0%). A specified minimum ground heat flux to the surface (25 W/m^2) is included. These specifications were chosen to produce as nearly as possible realistic simulations of the surface temperature magnitude and variation.

8.2.1. Background Profiles

Following the procedure discussed in detail by He et al., 2012, the geostrophic winds are modeled as the sum of a vertically invariant diurnally varying mean (U_{g0},V_{g0}) and a stochastic red *weather noise* component with zero mean and isotropic standard deviation (std(u), std(v)), and an autocorrelation timescale of 2 days, characteristic of the timescale associated with fluctuations of synoptic-scale pressure patterns in the midlatitudes. The effect of including this stochastic representation of weather variability for the effective pressure gradient force was discussed in some detail by He et al. (2012), also in the context of simulations of near surface wind statistics for the Cabauw site. It was found that the weather variability component substantially increases the climatological mean wind speed at all levels between the surface and 200 m, resulting in improved simulations of this variable as well as of the second and third moments of the wind speed distribution.

For simulations with diurnally varying clear-sky wind and temperature profiles the values of the mean geostrophic wind components are specified using the observed 5-year diurnally varying mean surface geostrophic wind in the clear-sky ensemble. The corresponding observed 5-year diurnal standard deviations of the wind components are used in the red-noise process simulation. However, additional simulations with fixed geostrophic winds were also carried out using the TKE scheme to obtain representative vertical profiles of the TKE budget terms and to study the nocturnal regimes discussed in section 8.2.3.

In all of the following analyses, the model is forced in a manner that is similar to that discussed in detail by He et al., 2012. The model is driven by a summertime mean diurnally varying incoming solar radiation at the top of the atmosphere. The initial and background temperature profile is defined by setting values as observed daily mean in the bottom 300 m. Above this level the background temperature decreases with height with a fixed lapse rate of 6.5 K/km to the 150-hPa level and then maintained at a constant value from 150 hPa to the top of the SCM at 50 hPa.

The initial and background specific humidity Q is set to the same dry clear-sky summertime profile that was used in He et al., 2012, with a maximum mean value of 8 g/kg at the lowest model level.

In the SCM simulations both air temperature and specific humidity are relaxed toward their background profiles with a relaxation timescale of 10 days. The duration of each simulation is 4 months (repetition of the May–August period), with the first month as a spin-up period and the remaining 3 months for analysis of near surface variable statistics. As we consider only clear-sky cases for this case study, cloudiness and precipitation are explicitly set to zero during each simulation.

The operational implementation in CanAM4 imposes a minimum background diffusivity (0.1 m^2/s) in the free atmosphere above the boundary layer. This minimum diffusivity setting has been retained in both the operational and TKE simulations to facilitate cleaner comparisons between them.

8.2.2. Cabauw Clear-Sky Simulation—Diurnal Cycle in the Lower 200 m

It is important to reiterate that we have intentionally chosen to compare results of SCM runs with observations in a climatological sense rather that for particular individual days as was done, for example, for the third GABLS Intercomparison, As noted above, the results presented here are from long SCM runs where the land surface scheme was fully active so that surface temperatures have also evolved with time and have come into equilibrium diurnal cycles that are consistent with the corresponding surface flux regimes. However, the salient features of stable nocturnal boundary layers that were a focus of the third GABLS Intercomparison are present in our simulations and are discussed on this section.

Figure 4 compares the simulated and observed diurnal cycle of wind speed and potential temperature in the lower 200 m for the Cabauw site. Results using both the operation CanAM4 boundary layer scheme and the

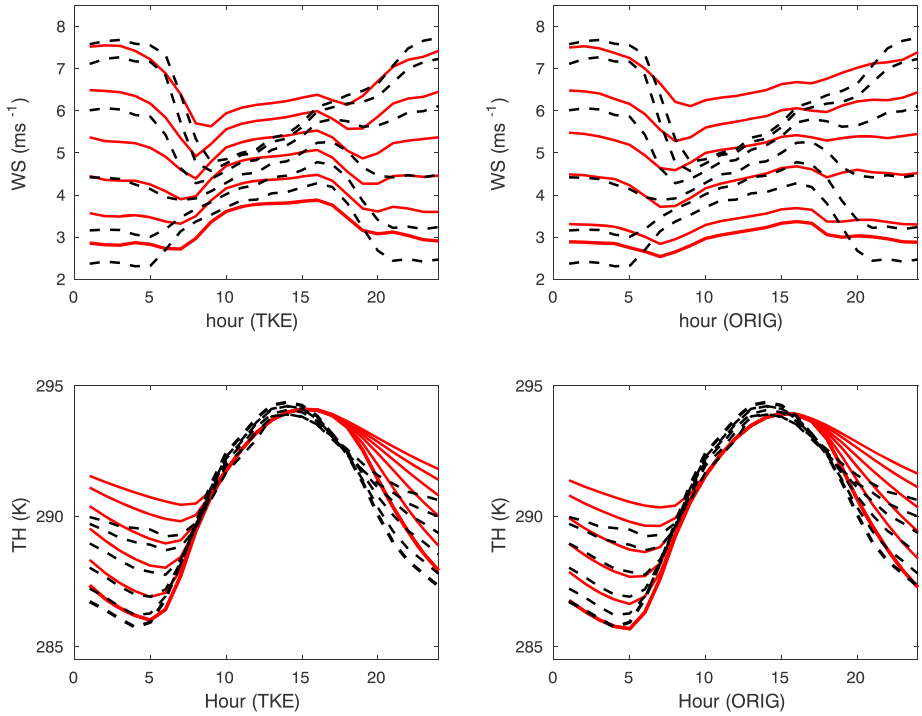

Figure 4. Comparison of clear-sky diurnal variations of near surface wind speed (WS) and potential temperature (TH) among observations (dashed), the operational CanAM4 boundary layer scheme (solid, right), and the TKE scheme (solid, left) at the at bottom six levels (10, 20, 40, 80, 140, and 200 m) of the Cabauw site during the season of JJA from 2007 to 2011. JJA = June-July-August; TKE = turbulent kinetic energy.

TKE version are shown. For comparison with observations at the Cabauw tower levels, simulated results for model levels are interpolated to the tower levels at 10, 20, 40, 80, 140, and 200 m.

Although both the operational and TKE schemes produce qualitatively similar simulations, there are notable differences. Wind speeds at the 10- and 20-m levels are maintained at values that are smaller and closer to each other for the operational scheme than for the TKE scheme. This is associated with larger diffusivities in daytime hours within the lower 200 m in the TKE scheme as illustrated in Figure 6. The wind speed at the 200-m level maximizes in the early morning hours in the observations and in both simulations. However, the nighttime wind speeds at the upper three levels are somewhat smaller in magnitude than observed. In contrast, during the night and early morning hours the mean wind speeds at the 10-m levels are larger than observed for both the TKE and operational schemes. In the later morning hours both schemes produce a transition to a reduced shear regime, qualitatively consistent with the observations, with larger wind speeds at the lower three levels and reduced speeds at the upper three levels. The wind shear remains stronger than observed, particularly in the upper four levels, for both the original and the TKE schemes. However, the TKE scheme maintains a weaker shear regime, in better agreement with the observations, during the daytime.

Both the operational and TKE schemes produce a transition to a well-mixed state for the potential temperature during the midmorning hours in good agreement with the observations. The nonlocal scheme produces homogeneous potential temperature profiles in the early afternoon for both the operational and TKE schemes, while the observed profiles remain slightly statically unstable in the lower 200 m of the boundary layer during this same time period.

The late afternoon transition to a stratified state is slightly delayed in the TKE simulation. This is most evident in the potential temperature structure for the bottom three levels shown in Figure 4. In this respect the performance of the TKE scheme is somewhat less realistic than the operational scheme. The nonlocal mixing shuts down for both the operational and TKE schemes in the late afternoon (near hour 18:00). The potential temperature is larger at all levels at that time for the TKE simulation. The surface temperature decreases

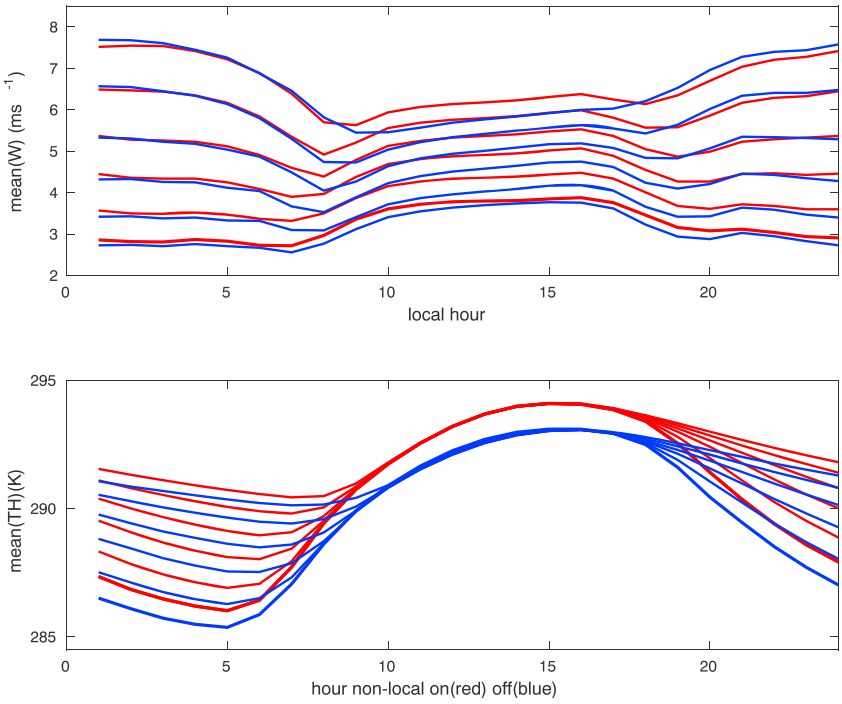

Figure 5. Simulated diurnal variation of the land surface temperatures for the Cabauw site during the JJA season. Black: operational scheme. Red: TKE scheme with the nonlocal mixing turned on. Blue: TKE scheme with the nonlocal mixing turned off. TKE = turbulent kinetic energy; JJA = June-July-August.

more rapidly for the TKE simulation (Figure 5) in association with the less efficient downward heat flux at the surface for stable conditions in the surface layer (Figure A1).

In both simulations the nighttime potential temperature stratification is stronger than observed. This structure is sensitive to the background potential temperature profile for the simulations. The observed structure may in part be associated with processes that are not included or accurately represented in the SCM configuration, possibly including the land surface and soil properties. However, although the lowest level is somewhat too warm in the TKE simulation, the bias in the nocturnal potential temperature structure is predominantly associated with excessively stable stratification, with the upper levels remaining somewhat too warm at night for both simulations. This could also be the result of eddy conductivities becoming too small in stable stratification. For the TKE scheme the main effect of the larger Prandtl numbers that occur in stable stratification is to reduce the diffusivity for potential temperature relative to that for momentum. The dissipation length scale also decreases rapidly in stable stratification for the TKE scheme. As noted in section 2 above, the Prandtl number for the operational scheme is unity in stable stratification. However, diffusivities, though remaining finite, decrease rapidly as a function of the gradient Richardson number in stable stratification (von Salzen et al., 2013 and references therein).

Baas et al. (2017) have modeled the mean and variability of the clear-sky statically stable nocturnal boundary layer structure at the Cabauw site using the TKE formulation of Baas et al. (2008). They use a linear relationship for the Prandtl number as a function of the gradient Richardson number with a limiting flux Richardson number of 0.5 (as compared to 0.25 for our formulation). Their simulated mean bulk stratification, represented as the difference between the potential temperature at the 200-m level and that at the 2-m level, is in good agreement with the observations, while their simulated 10-m winds and surface fluxes are slightly too large.

As noted above, the daytime well mixed state is sensitive to inclusion of the nonlocal mixing scheme. The TKE scheme does produce a nearly well mixed potential temperature structure in the absence of the nonlocal mixing (Figure 6). However, comparing Figures 4 and 6, it is seen to be less realistic in the middle of the

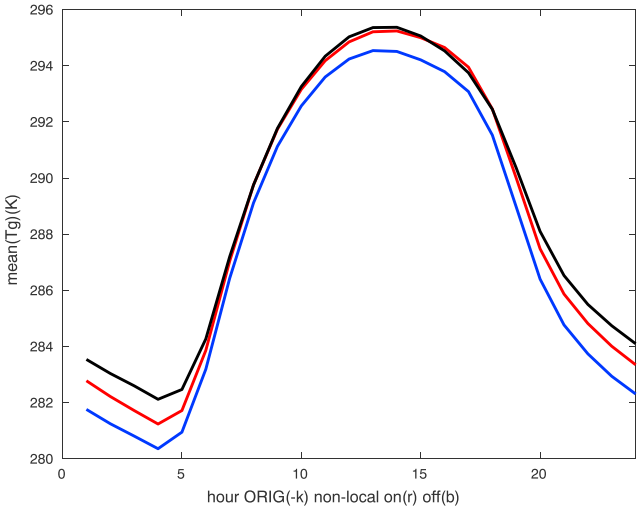

Figure 6. Simulated clear-sky diurnal variations of near surface wind speed and potential temperature at bottom six levels with (red) and without (blue) nonlocal mixing for the Cabauw site during the season of JJA from 2007 to 2011. JJA = June-July-August.

day when the strongest mixing occurs. The transition to the daytime well-mixed state is slightly slower and the daytime maximum potential temperature is slightly smaller in magnitude.

Of necessity, in absence of the nonlocal scheme, an upward buoyancy flux within the boundary layer can only be sustained if the stratification therein remains at least slightly statically unstable in the daytime. This promotes occurrence of slightly larger diffusivities within the lower part of the daytime boundary layer (not shown) resulting in a daytime wind speed profile with slightly reduced shear relative to that which occurs when the nonlocal mixing is included. However, although the somewhat larger eddy viscosity profiles that occur in the absence of the nonlocal mixing do give rise to reduced wind shear in the daytime, it is still larger than observed during the daytime hours when mixing is strongest.

It is also noteworthy that the temperatures are systematically smaller in magnitude for the entire diurnal cycle in the simulation without nonlocal mixing. Bearing in mind that Figure 6 depicts the simulated mean diurnal cycle, the larger temperatures that occur for the simulation with the nonlocal mixing, even for periods where it is not in operation, are indicative of a longer-term response to its presence when the boundary layer is convectively active. This is related to the smaller values of the simulated surface temperatures when the nonlocal scheme is turned off (Figure 5).

In contrast to the TKE scheme, the operational scheme does not realistically approximate a well-mixed state for the potential temperature during the daytime in the absence of the nonlocal mixing (not shown). Averaged vertical profiles of the diffusivities for momentum and scalar variables (temperature and specific humidity) during the daytime are depicted in Figure 7. Apart from the aforementioned enhanced values in the surface layer, diffusivities for the operational scheme are generally substantially smaller than those

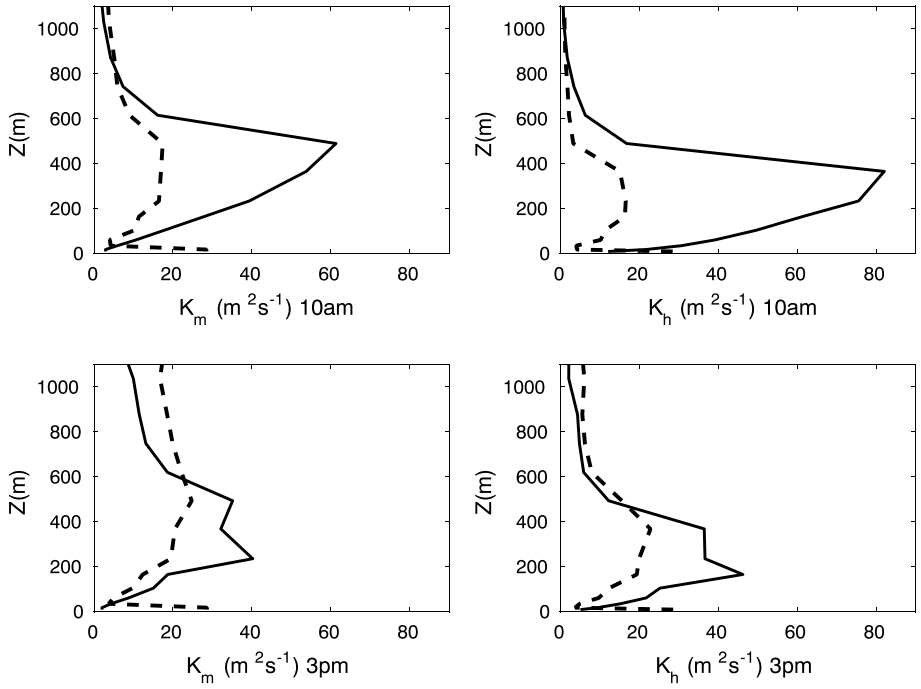

Figure 7. Vertical profiles of eddy viscosity (K_m) and conductivity (K_h) in the lower 1,000 m at midmorning and midafternoon for the Cabauw clear-sky simulation. Solid: TKE scheme, dashed: operational scheme. TKE = turbulent kinetic energy.

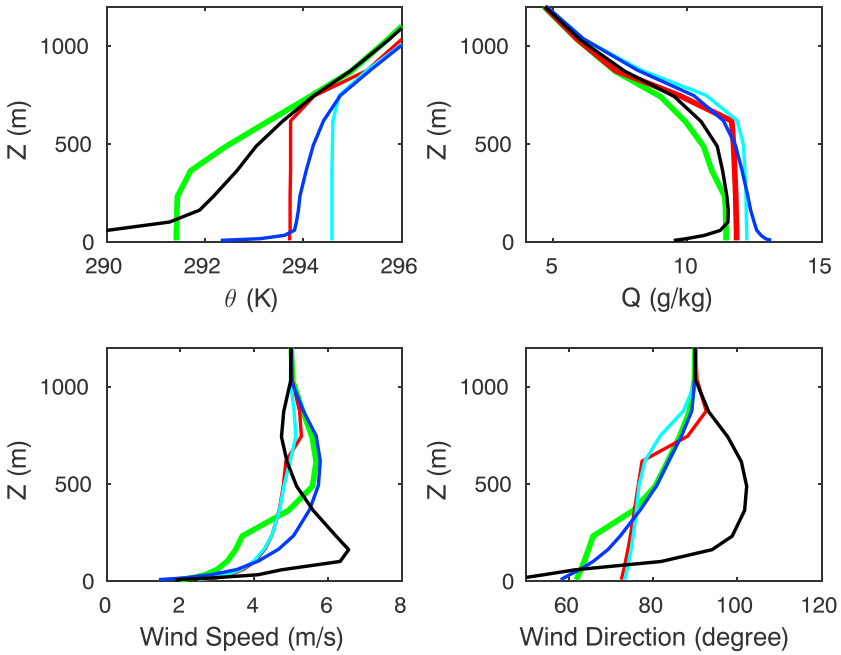

Figure 8. Simulated profiles in the boundary layer at selected hours of the diurnal cycle at the Cabauw Observatory in JJA for a uniform westerly geostrophic wind of 5 m/s. Hours are midnight (black), 09:00 (green), noon (red), 15:00 (cyan), 18:00 (blue). JJA = June-July-August.

for the TKE scheme within the boundary layer. Thus, although very effective mixing of potential temperature is accomplished by the nonlocal part of the scalar flux parameterization for both the operational and TKE schemes, the wind shear is larger in the daytime for the operational scheme (Figure 4 top right panel) consistent with the associated general smaller eddy viscosity values.

To illustrate the behavior of the simulated TKE budget in clear-sky convectively active conditions, the diurnal cycle simulation was repeated with a constant (5 m/s) westerly geostrophic wind without the red-noise weather variability process included. Vertical profiles of potential temperature, specific humidity, wind speed, and direction are shown for selected hours during the diurnal cycle in Figure 8. The TKE, dissipation length scale, and eddy viscosity for the subset of these hours during the daytime are shown in Figure 9. Corresponding components of the TKE budget are shown in Figure 10.

The development of a nocturnal jet structure is clearly evident in the midnight wind profiles (Figure 8). In contrast, the daytime wind structure shows reduced shear in association with the much larger eddy viscosity values that occur in the daytime boundary layer (Figure 9). The turbulence diminishes rapidly above the surface layer in the early evening when the surface-based inversion begins to develop again. The specific humidity is passive within the boundary layer and free atmosphere in this simulation as there are no clouds. The noon and midafternoon profiles reflect the effects of the nonlocal mixing scheme. The variation of the specific humidity near the surface reflects the effects of upward moisture flux in the daytime and downward flux at night.

The profiles of potential temperature and TKE budget components are qualitatively realistic when compared to similar results from other studies (e.g., Lenderink & Holtslag, 2004). The entrainment flux at the top of the daytime convective layer is perhaps slightly smaller than it should be (i.e., approximately 20% of the upward flux at the surface) for a typical convectively active boundary layer in clear-sky conditions. The entrainment flux is sensitive to both the magnitude of the entrainment diffusivity and to the rate of decrease of the mixing length with height in the stable capping region. These can be controlled to some extent by adjusting the free parameters (η,Λ_*) having in mind that both are also affected by the vertical resolution in that region.

8.2.3. Regime Transitions in the Nocturnal Boundary Layer

The phenomenon of transitions from weakly stable turbulent boundary layer regimes to strongly stable regimes within nocturnal boundary layers has been studied extensively over the past two decades. These

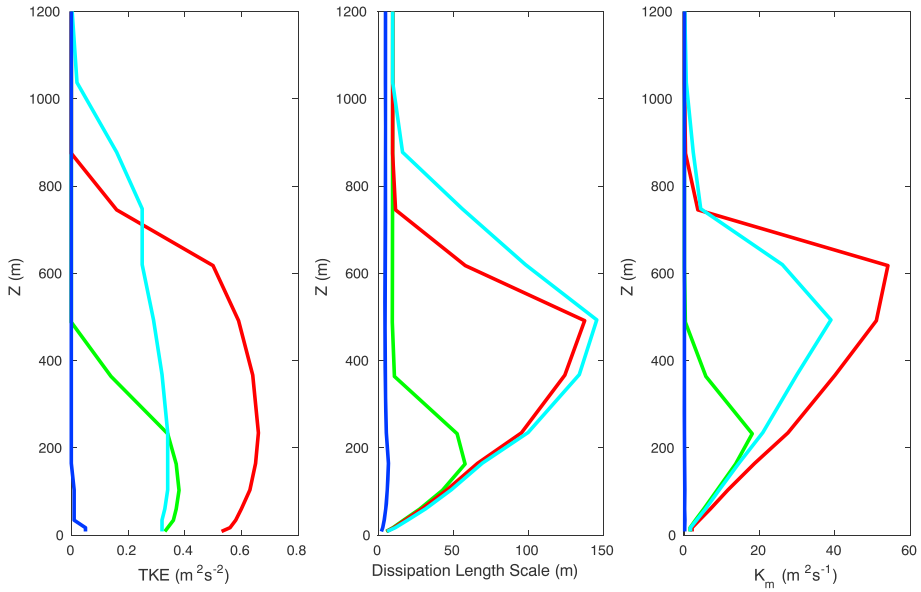

Figure 9. As in Figure 8 but for the daytime hours for turbulent kinetic energy, dissipation length scale, and eddy viscosity.

regime changes are characterized by rapid transitions from weakly stable moderately turbulent regimes to strongly stable regimes in which turbulence is very weak and intermittent. Such transitions typically occur within a narrow range of wind speeds near the top of the surface layer. Monahan et al. (2011, 2015) have shown that two distinct regimes with these characteristics commonly occur within the nocturnal boundary layer at the Cabauw, Netherlands site.

These studies support the regime transition mechanism that has been discussed extensively in a series of papers by Van de Wiel and coauthors (Van De Wiel et al., 2017 and references therein). This mechanism

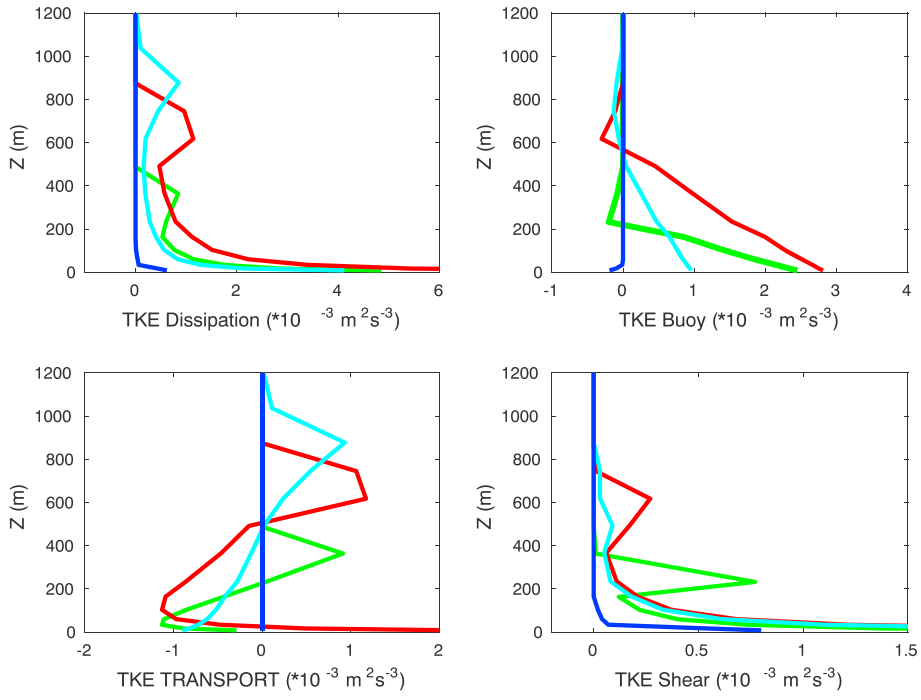

Figure 10. As in Figure 9 but for components of the turbulent kinetic energy budget. Top left, dissipation; top right, buoyancy production; bottom left, transport; bottom right, shear production.

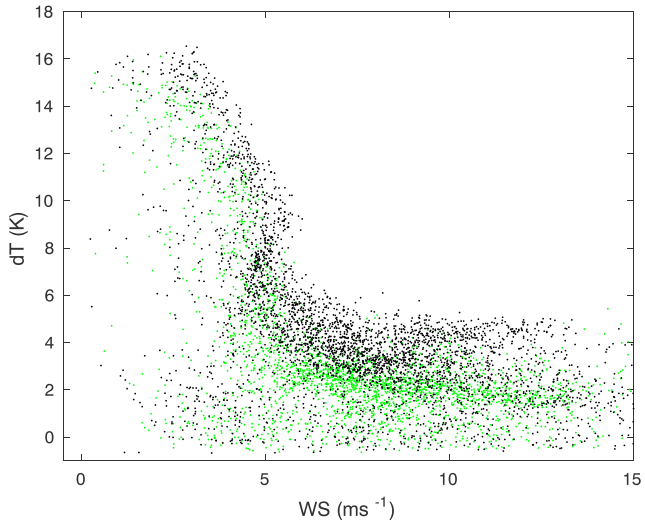

Figure 11. Simulated regime transition in the summertime clear-sky nocturnal boundary layer at the Cabauw, Netherlands site. Simulations are for the third level from the bottom (T3, nominally 35.8 m above the surface) of the 53-level configuration of the SCM. Black, TKE scheme; green, Operational CanAM4 scheme; Ordinate, difference between the air temperature and the land surface temperature (T3-Tg); Abscissa, corresponding wind speed at the third level. TKE = turbulent kinetic energy; SCM = single column model.

can be understood in terms of the maximum sustainable heat flux theory enunciated by these authors. In clear-sky conditions over land surfaces at night, a surface-based nocturnal inversion may become established through an imbalance between radiative cooling of the surface, upward conductive heat flux from the underlying soil layers, and downward turbulent sensible heat flux from the atmosphere. Theoretical and modeling studies suggest that a quasi-steady turbulent regime can exists for a given downward heat flux if the mechanical forcing (i.e., wind speed at the top of the idealized surface layer) is sufficiently large. Failing that, a *collapsed* regime in which turbulence is absent or weak and intermittent would be observed. Recent observational and modeling results largely support this conceptual framework for distinguishing between strong and weak turbulence regimes in stable nocturnal boundary layers (cf. Baas et al., 2017; Holdsworth et al., 2016; Monahan et al., 2015; Vignon et al., 2018).

Van De Wiel et al. (2017, hereinafter VdW) have presented analyses of nocturnal observations from Cabauw and observations from Dome C., Antarctica that show that transitions between turbulent and collapsed regimes typically occur within a relatively narrow range of wind speeds, in general agreement with the maximum sustainable heat flux framework (cf. their Figure 1). They note that some of the *long-tail* formulations typically used in GCMs do not produce transitions in a realistic manner (cf. their Figure 7).

In light of the foregoing, realistic representations of the turbulent and collapsed regimes in stable stratification may be of importance in both weather prediction and climate modeling. It is therefore of interest to examine how well the TKE-based formulation used herein reproduces the observed features of such regimes in a typical operational configuration. To illustrate this, results from two ensembles of five idealized nighttime clear-sky simulations using the 53-level configuration of the SCM are used. For comparison with observations shown in VdW for the 40-m level at the Cabauw site, we have selected results for the third level from the bottom in this configuration. This level is located approximately 35.8 m above the surface. For these simulations fixed geostrophic winds varying between 1 and 15 m/s were used. The land surface scheme was allowed to be fully coupled, but the soil moisture regime was taken to be typical of dry conditions. Simulations were performed using both the operational and TKE-based boundary layer schemes.

Figure 11 depicts the transition as a function of the temperature difference and wind speed for the SCM simulations. Both the operational and TKE schemes produce regime structures that are realistic and qualitatively similar to that observed at the Cabauw site (Figure 1 of VdW). Note that the temperature difference in Figure 1 of VdW is between the air temperature at 40 m and that at a level close to the surface, while that in Figure 8 is between the air temperature at the third model level and the surface temperature because the model configuration does not have a comparable near surface prognostic level. The surface temperature is determined as a prognostic variable within the land surface scheme by evaluating the surface energy budget.

Transitions from relatively strong to relatively weak inversions occur for a range of wind speeds that is similar in both simulations and observations. The simulated inversion strengths depicted in Figure 11 are on average apparently stronger than the observations as depicted in VdW, especially for the stronger inversion regime associated with weaker wind speeds. This is to be expected, at least qualitatively, due to our using the surface temperature instead of a near-surface air temperature to evaluate the bulk inversion strength. During nighttime there is typically a substantial (positive) difference between the near-surface air temperature and that at the land surface.

Although there is considerable overlap between the two simulations, on average the transition occurs at a slightly larger wind speed for the TKE scheme but in good agreement with the observations. Also, the inversion strength in the turbulent regime associated with higher wind speeds is larger for the TKE scheme

simulation. Both of these features are indicative of slightly reduced mixing efficiency of the TKE scheme, relative to the operational scheme, in the surface layer.

The operational CanAM4 land surface scheme was used herein with imposed relatively dry soil conditions. This has the effect of making the surface temperature more responsive to the net effects of radiative cooling and the downward turbulent sensible heat flux from the atmosphere. The associated simulated atmospheric nocturnal temperature regime is in general sensitive to surface and soil conditions. However, we have not explicitly explored this sensitivity extensively as doing so is beyond the scope of the work presented here. It is noteworthy in this regard that our results shown in Figure 8 are qualitatively similar to those of Baas et al. (2017) for their simulation with reduced skin-layer conductivity (their Figure 10).

8.3. DYCOMS-II Nocturnal Marine Stratocumulus

The study of Zhu et al. (2005, hereinafter Z05) compared the performance of a number of operational SCMs in simulations of nonprecipitating stratocumulus-topped boundary layers (STBLs) for the DYCOMS-II case study. This study was organized as part of the program of the Global Energy and Water Exchanges Cloud System Study. A corresponding group of LES simulations for this case study was documented by Stevens et al. (2005).

The Z05 study revealed that, given sufficient vertical resolution, all of the SCMs were able to reproduce key features of the idealized but realistic STBL in a manner qualitatively similar to observations and LES simulations. However, the SCM simulations showed substantially more variability and disagreement in their simulations of cloud water content as compared to LES simulations documented by Stevens et al. (2005). When the coarser vertical resolution typical of operational GCM configurations is used, the Z05 study revealed that this divergence among SCM simulations is substantially enhanced and, particularly in regard to cloud structure and liquid water path, the SCMs disagree markedly with each other and with LES simulations. These results point to key shortcomings in simulations of marine stratocumulus regimes.

Results from simulations using the SCM of the University of British Columbia were included in the Z05 study. The boundary layer, radiative transfer, and cloud schemes used in that SCM were adapted from those in an earlier developmental version of the CanAM4 model but were essentially the same as those in the current operational version used herein. This version exhibited many of the shortcomings in simulating STBL features documented in Z05. Therefore, we considered it interesting and instructive to repeat the DYCOMS-II case study to compare the performance of the TKE scheme with that of the current operational CanAM4 scheme.

The SCM simulations performed herein were carried out in accord with the specifications for experiment A in Z05, which in turn closely followed the specifications for the LES simulation in Stevens et al. (2005). The 53-level configuration was retained for the DYCOMS simulations for both the operational and TKE schemes. We present averaged results for hour 4 in the simulations for comparison with the published results of the aforementioned studies.

We also extended our simulations to longer periods to explore the possible development of an equilibrium cloud-topped boundary layer structure and compare aspects of the evolution and variability of the TKE and operational schemes on the context of the idealized DYCOMS-II case study configuration.

The simulated profiles of liquid water potential temperature, total water, liquid water, cloud cover, and horizontal wind components averaged over the fourth hour (shown in Figure 12), are comparable to similar profiles in the Z05 paper. The TKE scheme realistically maintains the well-mixed structure of vertical profiles of the liquid water potential temperature and total water within the boundary layer, and the strong, nearly discontinuous, gradients in these quantities within the capping inversion. In contrast, the operational scheme is less successful in maintaining a well-mixed structure for the total water (Figure 12).

Both schemes exhibit the elevated cloud and peaked liquid water profiles immediately below the capping inversion in a qualitatively realistic manner. The TKE scheme maintains narrower and more sharply peaked profiles for both of cloud cover and liquid water content. However, although the simulated liquid water profile for the TKE scheme is similar in structure to other SCM simulations, the peak liquid water amount is substantially larger than either observed or the LES simulated mean values (Z05, Figure 5). Typical peak values of the liquid water content for LES simulations are in the range of.3–.4 g/kg (Z05, Figure 1). The

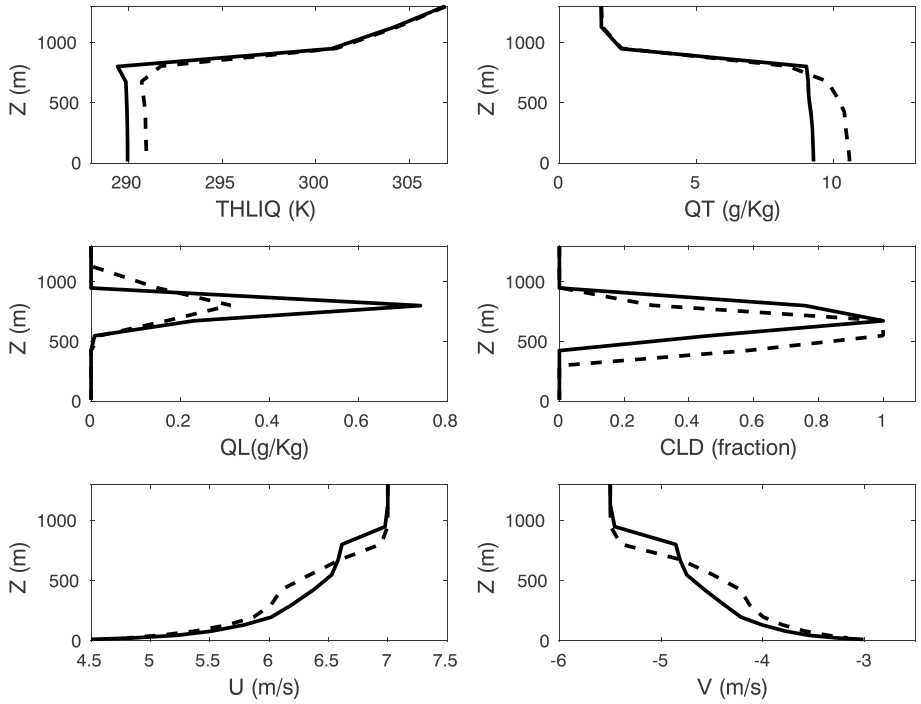

Figure 12. Profiles of the liquid water potential temperature (top left), total water (top right), liquid water (middle left), cloud cover (middle right), and the zonal and meridional components of the wind for the fourth hour of the DYCOMS-II simulation. Solid, TKE scheme; dashed,: operational scheme.

peak value for the operational scheme is within this range but that for the TKE scheme is larger by approximately a factor of 2 in the fourth hour.

Vertical profiles of the TKE and the dominant TKE budget terms are shown in Figure 13. These may be compared qualitatively with the LES simulation results documented by Stevens et al. (2005). As in the LES simulations, the dominant budget terms are the buoyancy production, TKE transport, and dissipation. The vertical profiles of the TKE and budget terms are qualitatively similar to those depicted in Figure C1 of Stevens et al. (2005) with peak values of the TKE and buoyancy production occurring in the cloud layer. However, the magnitudes for the TKE simulation are substantially larger than the corresponding LES simulation values. The excessive magnitude of the buoyancy production term, as the main source of turbulence in the cloud layer, is associated with excessive liquid water content as discussed above.

The sensitivity of the simulated values of liquid water to parameter settings in the cloud water to precipitation autoconversion rate parameterization was examined in separate simulations. As documented in von Salzen et al. (2013), the autoconversion rate parameterization in CanAM4 is based on Khairoutdinov and Kogan (2000) with an enhancement factor of 1.3 and a fixed specified global cloud droplet number concentration of 50 cm^{-3}. Reducing this value to 15 cm^{-3} reduced the peak liquid water content by 27% in the simulation with the TKE scheme.

We also tested the effects of varying the evaporative enhancement coefficient in the entrainment diffusivity in the range $0 \leq \alpha_{evp} \leq 30$. We found that the effect of this enhancement factor on the liquid water content was relatively small in our simulations with the maximum reduction of the peak liquid water content being typically less than 10% on average. It has a slightly more pronounced, but still relatively small, effect on the magnitude of the TKE and the buoyancy production and dissipation terms in the TKE budget within the cloud layer. These quantities are reduced in that region by about 10% on average by invoking the evaporative enhancement with the maximum value of the enhancement factor. The effect of reducing the cloud droplet concentration on these quantities is also more pronounced.

The profiles of cloud water and associated TKE budget terms are likely to be sensitive to vertical resolution and how the coupling between the cloud scheme and the TKE budget responds to resolution. By

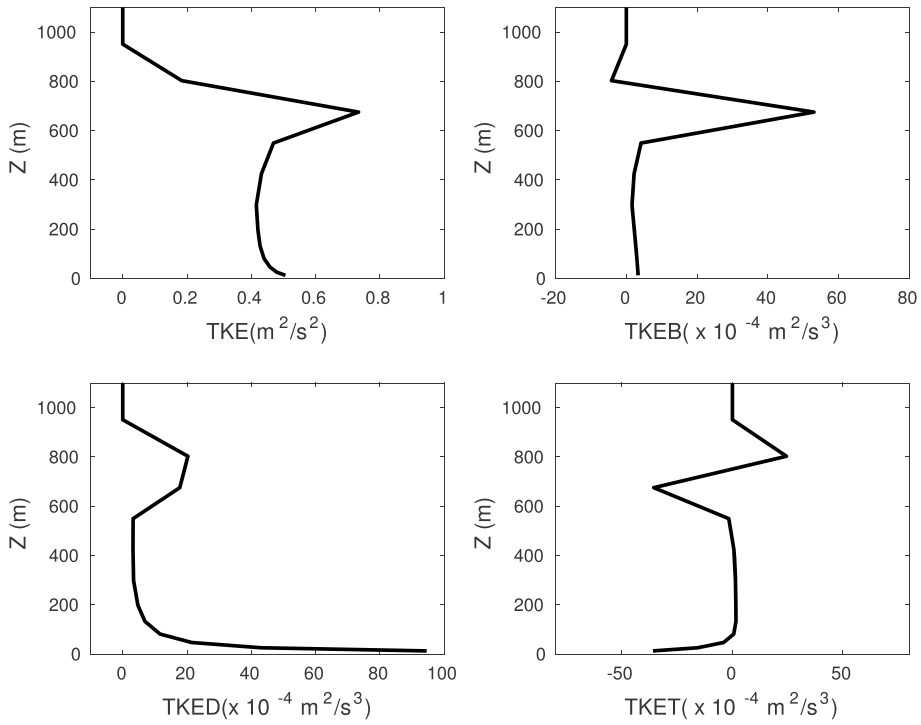

Figure 13. Turbulent kinetic energy (TKE) and the main TKE budget terms for hour 4 of the DYCOMS-II simulation. Budget terms are buoyancy production (TKEB), transport (TKET) and dissipation (TKED). DYCOMS-II = Second Dynamics and Chemistry of Marine Stratocumulus.

comparison, the coarse (L30) simulation of Bretherton and Park (2009) exhibits a larger buoyancy production over a deeper layer rather than a substantially larger peak value within the cloud layer. We have not attempted to evaluate the sensitivity to vertical resolution extensively here as we have preferred to carry out SCM tests using vertical level configurations that are the same as target GCM configurations. However, the vertical resolution in the region of the capping inversion is substantially coarser for the 53-level configuration used here than for the LES simulations.

The TKE and operational scheme simulations also differ markedly in respect of the simulated wind profiles. The TKE scheme averages for the fourth hour are qualitatively similar to results for other SCMs (Z05, Figure 3) with both components showing similar biases relative to LES profiles. The bias is somewhat more pronounced for the operational scheme. It is noted in Z05 that, in contrast to the LES simulations, which reach a quasi-steady state by hours 3–4, the SCM simulations are typically still evolving substantially at that stage in the simulations. This is also true for the SCM simulations here, particularly for the simulation using the operational scheme.

Profiles for the same variables are shown in Figure 14 for the thirtieth hour of the simulations using the TKE and operational schemes. By this time period the overall structures of the liquid water potential temperature, total water, and liquid water profiles for the TKE scheme simulation are qualitatively similar to those for the fourth hour, although all have clearly evolved to some extent. In contrast, the profiles for the simulation with the operational scheme have undergone marked changes by the thirtieth hour. An elevated cloud layer is maintained in the extended simulation with the TKE scheme. In contrast, for the operational scheme the boundary layer is fully occupied by cloud and the liquid water has increased substantially within the lower half of boundary layer with a secondary peak near the surface having developed. Consequently, the nearly well-mixed structure for the total water evident at the fourth hour is no longer present. This near-surface peak in the liquid water profile also contributes to the appearance of a local maximum in the liquid water potential temperature near the surface. Since the nonlocal mixing scheme does not operate within cloudy regions within the boundary layer, as noted in section 2.2.1 above, all of the turbulent mixing in these regions is associated with the local scheme.

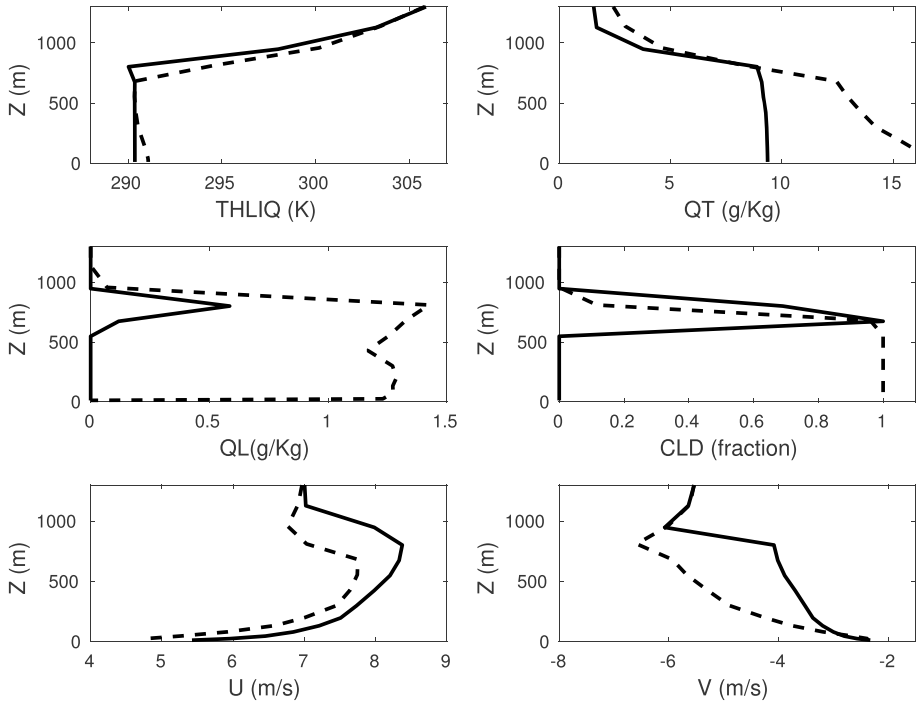

Figure 14. As in Figure 12 but for the thirtieth hour.

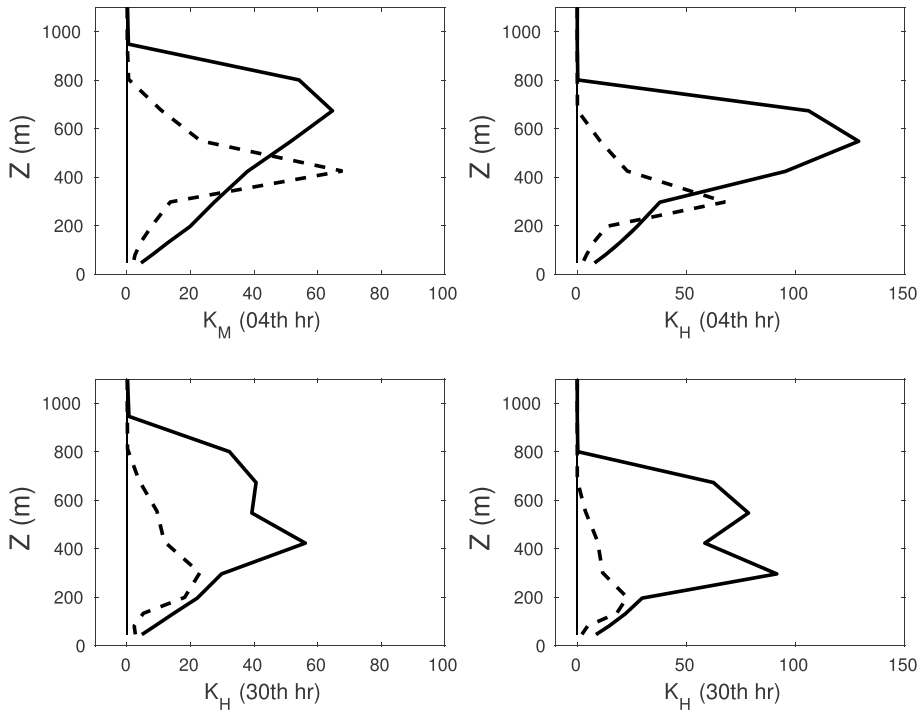

Figure 15. Eddy viscosity and heat conductivity profiles (m^2/s) for the DYCOMS-II simulation. Solid, TKE scheme; dashed, operational scheme. (top row) Average for hour 4; (bottom row) average for the thirtieth hour.
TKE = turbulent kinetic energy; DYCOMS-II = Second Dynamics and Chemistry of Marine Stratocumulus.

The mean wind profiles for the thirtieth hours of the simulations have clearly evolved from their structure for the fourth hour. The wind profiles within the boundary layer are qualitatively different for the simulation with the operational scheme. The magnitude of the zonal component has increased to exceed the geostrophic value at the top of the boundary layer for both simulations. However, the meridional component has decreased in magnitude for the TKE scheme but increased for the operational scheme.

The differences between the operational and TKE simulations are related to the differences in magnitudes of the turbulent diffusivities within the boundary layer. This further illustrated in Figure 15, which shows the vertical profiles of the diffusivities for the two simulations. The diffusivities remain relatively large throughout the boundary layer in the simulation with the TKE scheme but diminish with time in the simulation with the operational scheme.

The Coriolis force may act to produce inertial oscillations of the wind vector in circumstances where the effects of diffusive damping are relatively weak. There is evidence of this effect in the extended simulations (not shown). For both simulations the wind vector exhibited quasi-periodic fluctuations with a period of approximately 30 hr. However, the amplitude of the fluctuations was much smaller for the TKE scheme than for the operational scheme.

9. Discussion and Conclusions

A new scheme for representing the effects of turbulent transfer in the boundary layer and free atmosphere has been presented. This scheme has been implemented in the CanAM4 SCM, and its performance has been compared to that of the current operational scheme in CanAM4.

The new scheme utilizes the TKE budget in the context of a quasi-equilibrium formulation. The vertical transport of TKE is represented in terms of a nonlocal approach that is conceptually similar to that of Bretherton and Park (2009). Moist processes are dealt with in terms of quasi-conserved variables. Local contributions to the vertical turbulent transfer of momentum and conserved variables are represented in terms of eddy diffusivities based on the TKE using a simplified semi-empirical closure representation. This formulation takes into account recent observational and theoretical developments in regard to turbulence in stably stratified atmospheric boundary layers. Entrainment at the top of convectively active boundary layers is represented in terms of a local enhancement of the eddy diffusivity for scalar variables.

The relaxational treatment of nonlocal transfer of quasi-conserved scalar quantities in convectively active conditions within the boundary layer is based on that currently included in the operational CanAM4 scheme. This formulation has been adapted for use in the new TKE based scheme, and the associated contribution to buoyancy production is included in the TKE budget.

The performance of the TKE scheme has been evaluated and compared to that of the operational scheme for a series of SCM simulations for selected representative boundary layer regimes that may be encountered in practice in GCM applications. The configuration of the levels used in the SCM for most of the simulations is a possible future GCM configuration that will provide higher resolution in the lower 500 m than that of the current operational CanAM4 configuration.

The TKE scheme and the operational scheme perform in a qualitatively similar manner for simulations of the summertime diurnal cycle of winds and temperatures in clear-sky conditions in the lower 200 m of the Cabauw site. However, diffusivities above the surface layer, but within the boundary layer, for the new scheme are typically larger in the daytime hours and this produces slightly stronger (and more realistic) reductions of the vertical wind shear in the daytime.

In the absence of the nonlocal mixing scheme, the TKE scheme does produce nearly well mixed but slightly unstable profiles of potential temperature in the clear daytime boundary layer regimes. This is qualitatively in agreement with observations. However, potential temperatures are generally smaller than both the simulation where the nonlocal mixing is active and observations. This result is related to the different evolution of the surface temperature for these two cases. Space does not permit an extensive exploration and documentation, in this study, of the effects of different partitioning between the local and nonlocal components of the sensible heat flux profiles for daytime boundary layer regimes. However, it must also be noted that the local component, being dependent on the presence of small statically unstable potential temperature profiles in

the lower part of the boundary layer, is quite strongly sensitive to the model vertical resolution in that region. Earlier studies that were carried out during development work for CanAM4 and earlier versions of the GCM led to the conclusion that optimal performance requires that most of the sensible heat flux within the well mixed part of the boundary layer must be associated with the nonlocal scheme in these regimes. We have retained that partitioning here for the simulations with the nonlocal scheme turned on. However, this will be a topic for further exploration during testing of the TKE scheme in GCM simulations.

For stably stratified cloud-free nocturnal conditions, both the operational and TKE schemes produce qualitatively realistic simulations of relatively strongly turbulent regimes with weak shear within the surface layer and relatively weakly turbulent regimes with stronger shear.

The overall performance of the new TKE scheme and the operational scheme is comparable for hour 4 of the DYCOMS-II simulation. Both schemes utilize the operational CanAM4 cloud stratiform cloud scheme. However, the TKE scheme produces peak values of the liquid water content in hour 4 that are too large relative to LES simulations. The TKE budget shows that the corresponding buoyancy production is also too large relative to LES simulations. This points to issues concerning the interaction of the TKE scheme with the cloud scheme that is a topic for future investigation in the context of GCM applications.

Significant differences between the performance of the TKE scheme and the operational scheme are revealed in the extended DYCOMS-II simulations. For hour 30 of the DYCOMS-II simulations the TKE scheme maintains an elevated cloud layer within the boundary layer adjacent to the capping inversion with a peak water content that is of similar magnitude to that at hour 4. In contrast, for the corresponding simulation with the operational scheme, the boundary layer becomes fully cloudy by hour 30 with a substantially larger peak liquid water content.

In summary, except for peak liquid water contents in hour 4 of the DYCOMS-II simulation, the overall performance of the TKE scheme in the context of SCM simulations appears to be generally equal or superior to that of the operational scheme when compared to available observations and results of LES simulations. In practice some adjustments of parameters in the cloud scheme are likely to be required to achieve satisfactory overall performance in an operational implementation of the TKE scheme.

Comparison of the SCM clear-sky simulations with several years of data from the Cabauw Observatory, as discussed in section 8, has revealed some abiding shortcomings that are present in both the operational and TKE schemes. In particular, we have noted the larger than observed stratification during the nighttime and the larger than observed wind shear in the daytime hours. These are topics for future investigation. We have not carried out systematic testing of parameter settings with the SCM configuration used in this work. However, we anticipate carrying out such investigations in the course of GCM implementation and evaluation. The TKE scheme has recently been implemented in CanAM4. Testing and evaluation in the context of global climate simulations is currently under way.

Appendix 1: Solving the TKE Equation With Additional Forcing Terms A

Additional forcing terms in the TKE equation could arise from a variety of sources, such as nonlocal buoyancy production in the convectively active boundary layer and sporadic breaking of gravity waves in stably stratified regions. The corresponding additional forcing in the TKE equation is denoted symbolically as F and assumed here independent of k and k_* as a first approximation. Including this additional forcing term in the steady state TKE equation gives rise to the following equation:

$$\ell\frac{k^{1/2}}{c_0^{1/2}}F_m(1-Ri/\,\mathrm{Pr})S^2-\alpha\frac{\Lambda_* N}{c_o^{3/2}}k+F+\alpha\frac{k^{1/2}}{\ell}(k_*-k)-\frac{k^{3/2}}{c_0^{3/2}\ell}=0 \tag{A1.1}$$

Denoting $X=k^{1/2}$ for notational convenience, this equation can be written in the form:

$$X^3+\mu X^2-k_0X-F_*=0 \tag{A1.2}$$

In the context of this equation, where N is explicitly shown it is understood to be positive. Other parameters are defined as follows:

$$D = 1 + \alpha c_0^{3/2} \tag{A1.3}$$

$$k_0 = \left(\alpha c_0^{3/2} k_* + k_L\right)/D \tag{A1.4}$$

$$\mu = \alpha \Lambda_* N \ell / D \tag{A1.5}$$

$$F_* = \frac{\ell c_0^{3/2}}{D} F \tag{A1.6}$$

where k_L is the local equilibrium solution in the absence of forcing and transport.

A1.1 is formally a cubic equation for the TKE at a particular level, given k_*. However, the transport constraint (60) imposes a nonlocal implicit relationship between k and k_*. To determine both of these variables at all levels, we formally solve the cubic equation for interim values of k at each level using an estimated value of k_*. This interim profile is then used to determine k_* from equation (60). An efficient iterative scheme was constructed based on this procedure.

The cubic equation can be put into in a classical form by invoking the transformation

$$X = Z - \mu/3 \tag{A1.7}$$

Giving

$$Z^3 - pZ - q = 0 \tag{A1.8}$$

where $p = k_0 + \mu^3/3$, $q = F_* - (k_0 + 2\mu^2/9)\mu/3$.

The physically correct roots depend on the sign of the quantity:

$$\delta = q^2/4 - p^3/27 \tag{A1.9}$$

The physically correct solutions are

$$Z = \left(q/2 + \sqrt{\delta}\right)^{1/3} + \left(q/2 - \sqrt{\delta}\right)^{1/3}; \delta \geq 0 \tag{A1.10}$$

$$Z = \frac{2}{\sqrt{3}} p^{1/2} \cos\,\theta \;; \delta < 0 \tag{A1.11}$$

where

$$\theta = \frac{1}{3} \arcsin\left(\frac{|\delta|^{1/2}}{(q^2/4 + |\delta|)^{1/2}}\right) \tag{A1.12}$$

Appendix 2: Evaluation of the Surface Wind Stress and Heat Flux B

The lowest model level in typical GCM configurations is a few tens of meters above the surface (nominally 40 m above the local surface for the current operational version of CanAM4). In these circumstances MOST is used in an integrated sense to evaluate surface fluxes in terms of model prognostic variables at the lowest model level.

The basic features of the current operational implementation (Abdella & McFarlane, 1996) have been retained in this work. However, there are practical differences in the implementation for the stably stratified surface layer. Therefore, we confine attention to the evaluation of wind stress and sensible heat flux and moisture flux in those regimes. Turbulent fluxes of moisture and other scalar prognostic variable are treated similarly using dimensionless profile functions that are proportional to that for the sensible heat flux. In this appendix we sketch out the main features of changes to the surface flux calculations for stable conditions.

Following the notation of Abdella and McFarlane (1996) the magnitudes of the surface wind stress, τ_s, the turbulent sensible flux, $H_s = \rho_s\left(\overline{w'\theta}'\right)_s$, and the moisture flux $Q_s = \rho_s\left(\overline{w'q'}\right)_s$ (both positive when upward) are defined as

$$\tau_s = \rho_s u_*^2, H_s = -\rho_s c_p u_* \theta_*, Q_s = -\rho_s u_* q_* \tag{A2.1}$$

where ρ_s is the air density at the surface and c_p is the specific heat at constant pressure, θ is the potential temperature, and q is specific humidity. The MOST gradient profile relationship for virtual potential for the wind vector magnitude (U), potential temperature (θ), and specific humidity (q) in the surface layer is utilized in the form

$$\kappa z \partial U/\partial z = u_* \phi_m(\zeta), \;\; \kappa z \partial \theta/\partial z = \theta_* \phi_h(\zeta), \;\; \kappa z \partial q/\partial z = q_* \phi_h(\zeta) \tag{A2.2}$$

where $\zeta = z/L$ and, in accord with MOST, u_*, θ_*, and q_* are independent of height within the surface layer. Assuming that the neutral Prandtl number is unity and integrating these relationships between the surface and the lowest model level (located at $z = z_1$ where $U = U_1$, $\theta = \theta_1$) gives

$$u_* = \frac{\kappa U_1}{\ln\left(\frac{z}{z_0}\right) - [\Psi_m(\zeta_1) - \Psi_m(z_0/L)]} = \frac{\kappa U_1}{\Phi_m} \tag{A2.3}$$

$$\theta_* = \frac{\kappa(\theta_1 - \theta_s)}{\ln\left(\frac{z_1}{z_t}\right) - [\Psi_h(\zeta_1) - \Psi_h(z_t/L)]} = \frac{\kappa(\theta_1 - \theta_s)}{\Phi_h} \tag{A2.4}$$

$$q_* = \frac{\kappa(q_1 - q_s)}{\ln\left(\frac{z_1}{z_t}\right) - [\Psi_h(\zeta_1) - \Psi_h(z_t/L)]} = \frac{\kappa(q_1 - q_s)}{\Phi_h} \tag{A2.5}$$

where z_0 and z_t are, respectively, roughness lengths for momentum and potential temperature and humidity (assumed here to be the same as that for potential temperature). The integrated profile functions are defined as

$$\Psi_m(\zeta) = \int\left[\frac{1-\phi_m(\zeta)}{z}\right]dz \;\;, \;\; \Psi_h(\zeta) = \int[(1-\phi_h(\zeta))/z]dz \tag{A2.6}$$

For the stable side, using equations (22a) and (22b):

$$\Psi_m = -4\zeta \;\;, \;\; \Psi_h = -(1 + 8\zeta/3)^{3/2} \tag{A2.7}$$

The turbulent buoyancy flux within the surface layer is given approximately by $\overline{w'\theta_v'} = -u_*\left[\theta_* + 0.61(\theta_v)_1 q_*\right]$. To a good approximation, this satisfies essentially the same MOST flux relationship as that for the sensible heat flux. A relationship between these stability functions and the bulk Richardson number for the surface layer is then given by

$$Ri_B = \frac{g z_1\left[(\theta_v)_1 - (\theta_v)_s\right]}{(\theta_v)_1 U_1^2} = \zeta_1 \frac{\Phi_h}{\Phi_m^2} \tag{A2.8}$$

Following a similar procedure to that of Abdella and McFarlane (1996) we use this relationship to express ζ_1 in terms of Ri_B. This relationship is nonlinear. However, we have found that the following approximation is quite accurate for a wide range of positive values of the bulk Richardson number:

$$\zeta_1 = Ri_B(A_1 + A_2 Ri_B) \tag{A2.9}$$

where $A_1 = [ln(z_1/z_0)]^2 / \, ln\,(z_1/z_t)$, $A_2 = (27/2)(1 - z_0/z_1)^4/[1 - (z_t/z_1)^{3/2}]^2$.

Figure A1 shows the effects of the change in the surface layer formulation on the surface drag and heat flux coefficients. As compared to the operational CanAM4 formulation (von Salzen et al., 2013, Abdella and McFarlane, 1996), the revised formulation results in a more rapid decay of these quantities with increasing values of the surface layer bulk Richardson number.

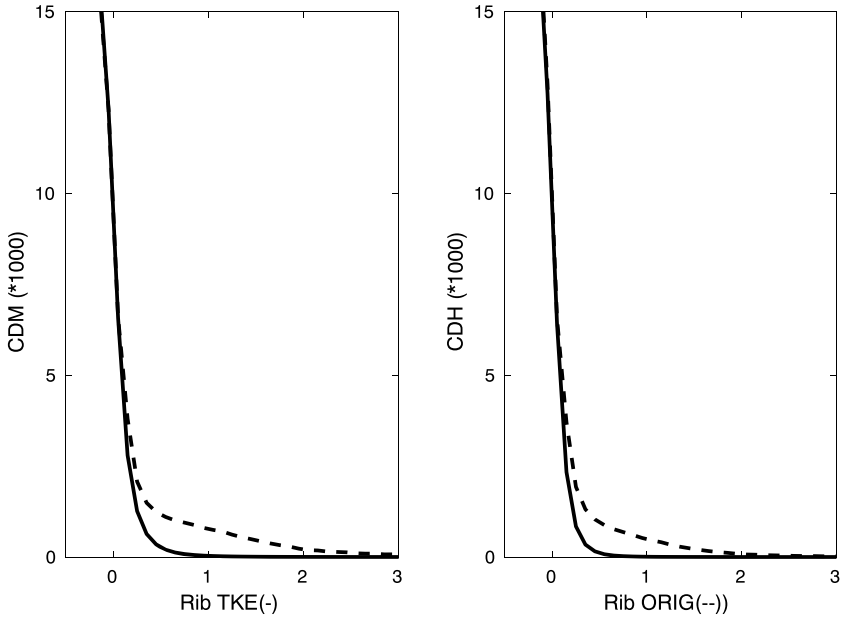

Figure A1. Comparison of the operational (dashed) and revised (solid) formulations for the surface drag and heat flux coefficients as a function of the bulk Richardson number for stable conditions.

Acknowledgments
During the course of this work Y. He was supported under the Canadian Network for Regional Climate and Weather Processes grant 433915-2012 awarded by the Natural Sciences and Engineering Research Council of Canada. A. Monahan acknowledges support from the Discovery Grant program of the Natural Sciences and Engineering Research Council of Canada. Data from the Cabauw tower is accessible and can be downloaded from the Cabauw Experimental Site for Atmospheric Research (CESAR) http://www.cesar-database.nl/. The corresponding surface geostrophic wind data used in this study were provided by Fred Bosveld of the Royal Netherlands Meteorological Institute.
The authors are grateful to Knut von Salzen and two anonymous reviewers for providing valuable comments that have helped to improve the manuscript.

References

Abdella, K., & McFarlane, N. A. (1996). Parameterization of the surface-layer exchange coefficients for atmospheric models. *Boundary-Layer Meteorology*, *80*(3), 223–248. https://doi.org/10.1007/BF00119544

Abdella, K., & McFarlane, N. A. (2001). Modelling boundary-layer clouds with a statistical cloud scheme and a second-order turbulence closure. *Boundary-Layer Meteorology*, *98*(3), 387–410. https://doi.org/10.1023/A:1018714808499

Baas, P., deRoode, S. R., & Lenderink, G. (2008). The scaling behavior of a turbulent kinetic energy closure model for stably stratified conditions. *Boundary-Layer Meteorology*, *127*(1), 17–36. https://doi.org/10.1007/s10546-007-9253-y

Baas, P., van de Wiel, B. J. H., Van der Linden, S. J. A., & Bosveld, F. C. (2017). From near-nuetral to strongly stratified: Adequately modelling the clear-sky nocturnal boundary layer at Cabauw. *Boundary-Layer Meteorology*, *166*, 217–238.

Beljaars, A. C. M. (1994). The parametrization of surface fluxes in large-scale models under free convection. *Quarterly Journal of the Royal Meteorological Society*, *121*, 255–270.

Beljaars, A. C. M., & Holtslag, A. A. M. (1991). Flux parameterization over land surface for atmospheric models. *Journal of Applied Meteorology*, *30*(3), 327–341. https://doi.org/10.1175/1520-0450(1991)030<0327:FPOLSF>2.0.CO;2

Bosveld, F. C., Baas, P., van Mejgaard, E., de Bruijn, E. I. F., Steeneveld, G.-J., & Holtslag, A. A. M. (2014). Intercomparison case for evaluation studies of boundary-layer models. Part A: Case selection and set-up. *Boundary-Layer Meteorology*, *152*(2), 133–156. https://doi.org/10.1007/s10546-014-9917-3

Bretherton, C. S., & Park, S. (2009). A new moist turbulence parameterization in the community atmosphere model. *Journal of Climate*, *22*(12), 3422–3448. https://doi.org/10.1175/2008JCLI2556.1

Canuto, V. M., Cheng, Y., & Howard, A. M. (2007). Non-local ocean mixing model and a new plume model for deep convection. *Ocean Model*, *16*(1-2), 28–46. https://doi.org/10.1016/j.ocemod.2006.07.003

Canuto, V. M., Cheng, Y., Howard, A. M., & Esau, I. N. (2008). Stably stratified flows: A model with No Ri (cr). *Journal of the Atmospheric Sciences*, *65*(7), 2437–2447. https://doi.org/10.1175/2007JAS2470.1

Cheng, Y., Canuto, V. M., & Howard, A. M. (2004). Reply. *Journal of the Atmospheric Sciences*, *61*(10), 1200–1204. https://doi.org/10.1175/1520-0469(2004)061<1200:R>2.0.CO;2

Cheng, Y., Canuto, V. M., & Howard, A. M. (2005). Nonlocal convective PBL model based on new third- and fourth-order moments. *Journal of the Atmospheric Sciences*, *62*(7), 2189–2204. https://doi.org/10.1175/JAS3474.1

Cuxart, J., Bougeault, P., & Redelsperger, J. L. (2000). A turbulence scheme allowing for mesoscale and large-eddy simulations. *Quarterly Journal of the Royal Meteorological Society*, *126*(562), 1–30. https://doi.org/10.1002/qj.49712656202

Deardorff, J. W. (1980). Stratocumulus-capped mixed layers derived from a three-dimensional model. *Boundary-Layer Meteorology*, *18*(4), 495–527. https://doi.org/10.1007/BF00119502

Dyer, A. J. (1974). A review of flux-profile relationships. *Boundary-Layer Meteorology*, *7*(3), 363–372. https://doi.org/10.1007/BF00240838

Esau, I. N., & Grachev, A. (2007). Turbulent Prandtl number in stably stratified atmospheric boundary layer: Intercomparison between LES and SHEBA data, e-. *WindEng*, *5*, 1–17. ISSN 1901–9181

Ferrero, E., Quan, L. H., & Massone, D. (2011). Turbulence in the stable boundary layer at higher Richardson numbers. *Boundary Layer Meteorology*, *139*(2), 225–240. https://doi.org/10.1007/s10546-010-9581-1

Grachev, A. A., Andreas, E. L., Fairall, C. W., Guest, P. S., & Persson, P. O. G. (2013). The critical Richardson number and limits of applicability of local similarity theory in the stable boundary layer. *Boundary Layer Meteorology*, *147*(1), 51–82. https://doi.org/10.1007/s10546-012-9771-0

He, Y., McFarlane, N., & Monahan, A. H. (2012). The influence of boundary layer processes on the diurnal variation of the climatological near-surface wind speed probability distribution over land. *Journal of Climate*, *25*(18), 6441–6458. https://doi.org/10.1175/JCLI-D-11-00321.1

Hogstrom, U. (1988). Non-dimensional wind and temperature profiles in the atmospheric surface layer—A re-evaluation. *Boundary Layer Meteorology*, *42*(1-2), 55–78. https://doi.org/10.1007/BF00119875

Hogstrom, U. (1996). Review of some basic characteristics of the atmospheric surface layer. *Journal of the Atmospheric Sciences*, *78*(3-4), 215–246. https://doi.org/10.1007/BF00120937

Holdsworth, A. M., Rees, T., & Monahan, A. H. (2016). Parameterization sensitivity and instability characteristics of the maximum sustainable heat flux framework for predicting turbulent collapse. *Journal of Atmospheric Science*, *73*(9), 3527–3540.

Holtslag, A. A. M., & Moeng, C. H. (1991). Eddy diffusivity and countergradient transport in the convective atmospheric boundary layer. *Journal of the Atmospheric Sciences*, *48*(14), 1690–1698. https://doi.org/10.1175/1520-0469(1991)048<1690:EDACTI>2.0.CO;2

Kantha, L., & Carniel, S. (2009). A note on modeling mixing in stably stratified flows. *Journal of the Atmospheric Sciences*, *66*(8), 2501–2505. https://doi.org/10.1175/2009JAS3041.1

Khairoutdinov, M., & Kogan, Y. (2000). A new cloud physics parameterization in a large-eddy simulation model of marine stratocumulus. *Monthly Weather Review*, *128*(1), 229–243.

Kosovic, B., & Curry, J. A. (2000). A large eddy simulation study of a quasi-steady, stably stratified atmospheric boundary layer. *Journal of the Atmospheric Sciences*, *57*(8), 1052–1068. https://doi.org/10.1175/1520-0469(2000)057<1052:ALESSO>2.0.CO;2

Lappen, C.-L., & Randall, D. A. (2001). Toward a unified parameterization of the boundary layer and moist convection. Part I: A new type of mass-flux model. *Journal of the Atmospheric Sciences*, *58*(15), 2021–2036. https://doi.org/10.1175/1520-0469(2001)058<2021:TAUPOT>2.0.CO;2

Larsen, V. E., & Golaz, J.-C. (2005). Using probability density functions to derive consistent closure relationships among higher-order moments. *Monthly Weather Review*, *133*(4), 1023–1042. https://doi.org/10.1175/MWR2902.1

Lenderink, G., & Holtslag, A. A. M. (2004). An updated length-scale formulation for turbulent mixing in clear and cloudy boundary layer. *Quarterly Journal of the Royal Meteorological Society*, *130*(604), 3405–3427. https://doi.org/10.1256/qj.03.117

Li, D., Katul, G. G., & Zilitinkevich, S. S. (2015). Revisiting the turbulent Prandtl number in an idealized atmospheric surface layer. *Journal of the Atmospheric Sciences*, *72*(6), 2394–2410. https://doi.org/10.1175/JAS-D-14-0335.1

Mauritsen, T., & Svensson, G. (2007). Observations of stably stratified shear-driven atmospheric turbulence at low and high Richardson numbers. *Journal of the Atmospheric Sciences*, *57*(2), 645–655.

Mellor, G. L. (1989). *Retrospective on ocean boundary layer modeling and second moment closure. Proc. Fifth Aha Huliko'a Hawaiian Winter Workshop* (pp. 251–272). Honolulu, HI: Hawaii Institute of Geophysics.

Mellor, G. L., & Yamada, T. (1974). A hierarchy of turbulence closure models for planetary boundary layers. *Journal of the Atmospheric Sciences*, *31*(10), 1791–1806.

Mellor, G. L., & Yamada, T. (1982). Development of a turbulence closure model for geophysical fluid problems. *Review of Geophysics*, *20*(4), 851–875. https://doi.org/10.1029/RG020i004p00851

Mirocha, J. D., & Kosovic, B. (2010). A large-eddy simulation study of the influence of subsidence on the stably stratified atmospheric boundary layer. *Boundary-Layer Meteorology*, *134*(1), 1–21. https://doi.org/10.1007/s10546-009-9449-4

Monahan, A. M., He, Y., McFarlane, N., & Dai, A. (2011). The probability distribution of global land surface wind speed. *Journal of Climate*, *24*(15), 3892–3909. https://doi.org/10.1175/2011JCLI4106.1

Monahan, A. M., Rees, T., He, Y., & McFarlane, N. (2015). Multiple regimes of wind, stratification, and turbulence in the stable boundary layer. *Journal of the Atmospheric Sciences*, *72*(8), 3178–3198. https://doi.org/10.1175/JAS-D-14-0311.1

Nakanishi, M. (2001). Improvement of the Mellor-Yamada turbulence closure model based on large-eddy simulation data. *Boundary-Layer Meteorology*, *99*(3), 349–378. https://doi.org/10.1023/A:1018915827400

Otte, M., & Wyngaard, J. C. (2001). Stably stratified interfacial-layer turbulence from large-eddy simulation. *Journal of the Atmospheric Sciences*, *58*(22), 3424–3442. https://doi.org/10.1175/1520-0469(2001)058<3424:SSILTF>2.0.CO;2

Richardson, H., Baas, s., & Holtslag, A. A. M. (2013). Improving stable boundary-layer height estimation using a stability-dependent critical bulk Richardson number. *Boundary-Layer Meteorol*, *148*, 93–109.

Schubert, W. H., Wakefield, J. S., Steiner, E. J., & Cox, S. K. (1979). Marine stratocumulus convection. Part I: Governing equations and horizontally homogeneous solutions. *Journal of the Atmospheric Sciences*, *36*(7), 1286–1307. https://doi.org/10.1175/1520-0469(1979)036<1286:MSCPIG>2.0.CO;2

Schumann, U. (1991). Subgrid length-scales for large-eddy simulation of stratified turbulence. *Theoretical and Computational Fluid Dynamics*, *2*(5-6), 279–290. https://doi.org/10.1007/BF00271468

Siebesma, A. P., Soares, P. M. M., & Teixeira, J. (2007). A combined eddy-diffusivity mass-flux approach for the convective boundary layer. *Journal of Atmospheric Science*, *64*(7), 1230–1248.

Stevens, B., Moeng, C. H., Ackerman, A. S., Bretherton, C. S., Chlond, A., de Roode, S., et al. (2005). Evaluation of large-eddy simulations via observations of nocturnal marine stratocumulus. *Monthly Weather Review*, *133*(6), 1443–1462., 6061. https://doi.org/10.1175/MWR2930.1

Sus˘elj, K., Teixeira, J., & Matheou, G. (2012). Eddy diffusivity/mass flux and shallow cumulus boundary layer: An updraft PDF multiple mass flux scheme. *Journal of the Atmospheric Sciences*, *69*(5), 1513–1533. https://doi.org/10.1175/JAS-D-11-090.1

Van De Wiel, Bas, J. H., Vignon, E., Baas, P., Van Hooijdonk, I. G. S., Van der Linden, S. J. A., et al. (2017). Regime transitions in near-surface temperature inversions: A conceptual model. *Journal of the Atmospheric Sciences*, *74*(4), 1057–1073. https://doi.org/10.1175/JAS-D-16-0180.1

Venayagamoorthy, S. K., & Stretch, D. D. (2010). On the turbulent Prandtl number in homogeneous stably stratified turbulence. *Journal of Fluid Mechanics*, *644*, 359–369. https://doi.org/10.1017/S002211200999293X

Vignon, E., Hourdin, F., Genthon, C., Van de Wiel, B. J. H., Gallee, H., Madeleine, J.-B., & Beaumet, J. (2018). Modeling the dynamics of the atmospheric boundary layer over the Antarctic plateau with a general circulation model. *Journal of Advances in Modeling Earth Systems*, *10*(1), 98–125. https://doi.org/10.1002/2017MS001184

von Salzen, K., Scinocca, J. F., McFarlane, N. A., Li, J., Cole, J. N. S., Plummer, D., et al. (2013). The Canadian Fourth Generation Atmospheric Global Climate Model (CanAM4), Part I: Representation of physical processes. *Atmosphere–Ocean*, *51*(1), 104–125. https://doi.org/10.1080/07055900.2012.755610

Witek, M. L., Teixeira, J., & Matheou, G. (2011). An eddy diffusivity-mass flux approach to the vertical transport of turbulent kinetic energy in convective boundary layers. *Journal of the Atmospheric Sciences*, *68*(10), 2385–2394. https://doi.org/10.1175/JAS-D-11-06.1

Zhu, P., Bretherton, C. S., Köhler, M., Cheng, A., Chlond, A., Geng, Q., et al. (2005). Intercomparison and interpretation of single-column model simulations of a nocturnal stratocumulus-topped marine boundary layer. *Monthly Weather Review*, *133*(9), 2741–2758. https://doi.org/10.1175/MWR2997.1

Zilitinkevich, S. S., Elperin, T., & Kleeorin, N. (2008). Turbulence energetics in stably stratified geophysical flows: Strong and weak mixing regimes. *Quarterly Journal of the Royal Meteorological Society*, *633*, 793–799.

Zilitinkevich, S. S., Elperin, T., Kleeorin, N., & Rogachevskii, I. (2007). Energy- and flux-budget (EFB) turbulence closure model for the stably stratified flows. Part I: Steady-state, homogeneous regimes. *Boundary-Layer Meteorology*, *125*(2), 167–191. https://doi.org/10.1007/s10546-007-9189-2

Zilitinkevich, S. S., Elperin, T., Kleeorin, N., Rogachevskii, I., & Esau, I. (2013). A hierarchy of energy-and flux-budget (EFB) turbulence closure models for stably-stratified geophysical flows. *Boundary-Layer Meteorology*, *146*(3), 341–373. https://doi.org/10.1007/s10546-012-9768-8

Zilitinkevich, S. S., Hunt, J. C. R., Grachev, A. A., Esau, I. N., Lalas, D. P., Akylas, E., et al. (2006). The influence of large convective eddies on the surface layer turbulence. *Quarterly Journal of the Royal Meteorological Society*, *132*(618), 1423–1456. https://doi.org/10.1256/qj.05.79